Characterization of Ingestion through the Rim Seal of Rotor-Stator Disk Cavity in

a Subscale Single-Stage Axial Turbine

by

Prashant Singh

A Thesis Presented in Partial Fulfillment
of the Requirements for the Degree
Master of Science

Approved June 2014 by the
Graduate Supervisory Committee:

Ramendra P. Roy, Co-Chair
Marc Mignolet, Co-Chair
Taewoo Lee

ARIZONA STATE UNIVERSITY

August 2014

ABSTRACT

In order to achieve higher gas turbine efficiency, the main gas temperature at turbine inlet has been steadily increased from approximately 900°C to about 1500°C over the last few decades. This temperature is higher than the maximum acceptable temperature for turbine internals. The hot main gas may get ingested into the space between rotor and stator, the rotor-stator disk cavity in a stage because of the pressure differential between main gas annulus and the disk cavity. To reduce this ingestion, the disk cavity is equipped with a rim seal; additionally, secondary (purge) air is supplied to the cavity. Since the purge air is typically bled off the compressor discharge, this reducing the overall gas turbine efficiency, much research has been carried out to estimate the minimum purge flow necessary ($c_{w,min}$) for complete sealing of disk cavities.

In this work, experiments have been performed in a subscale single-stage axial turbine featuring vanes, blades and an axially-overlapping radial-clearance seal at the disk cavity rim. The turbine stage is also equipped with a labyrinth seal radially inboard. The stage geometry and the experimental conditions were such that the ingestion into the disk cavity was driven by the pressure asymmetry in the main gas annulus. In the experiments, time-averaged static pressure was measured at several locations in the main annulus and in the disk cavity; the pressure differential between a location on the vane platform close to lip (this being the rim seal part on the stator) and a location in the 'seal region' in the cavity is considered to be the driving potential for both ingestion and egress. Time-averaged

i

volumetric concentration of the tracer gas (CO_2) in the purge air supplied was measured at multiple radial locations on the stator surface. The pressure and ingestion data were then used to calculate the ingestion and egress discharge coefficients for a range of purge flow rates, employing a simple orifice model of the rim seal. For the experiments performed, the egress discharge coefficient increased and the ingestion discharge coefficient decreased with the purge air flow rate. A method for estimation of $c_{w,min}$ is also proposed.

To,

My parents

Shri Harsh Vardhan Singh,

Shrimati Bina Singh

and my lovely sister Neha.

ACKNOWLEDGEMENTS

TABLE OF CONTENTS

LIST OF TABLES

LIST OF FIGURES

NOMENCLATURE

Δa: area integral [Fig. **4.2**]

A_{gap}: area of rim seal gap over entire circumference (m^2)

C: CO_2 time-averaged mass concentration (%)

C_d: discharge coefficient

C_{di}, C_{de}: discharge coefficients for ingestion, egress through rim seal

C_{vax}: vane axial chord length

c_w: dimensionless mass flow rate of purge air, $= \dot{m}_{purge}/\mu R_h$

$c_{w,egress}$: dimensionless mass flow rate of egress air, $= \dot{m}_{egress}/\mu R_h$

$c_{w,fd}$: dimensionless free disk pumping mass flow rate of air, $=0.219Re_\phi{}^{0.8}$

cfm: cubic feet per minute

$\dot{m}$: mass flow rate of air (kg/s)

G_c: dimensionless rim seal radial gap, $=s_c/R_h$

Δp: pressure differential between main gas path and rim cavity (Pa)

Q: volumetric flow rate (m^3/s, cfm)

r: radial coordinate with origin at rotor/stator centerline

r: position vector

R_h: vane/blade hub radius (m)

Re_{R_h}: main air flow Reynolds number based on R_h, $= \rho V_{ax} R_h / \mu$

Re_{vax}: main air flow Reynolds number based on C_{vax}, $= \rho V_{ax} C_{vax} / \mu$

Re_ϕ: rotor disk rotational Reynolds number, $= \rho \Omega R_h^2 / \mu$

rpm: revolutions per minute

s: axial gap between rotor and stator disks (mm)

s_c: rim seal radial gap (mm)

U: blade hub speed (m/s)

V_{ax}: mixed-mean axial velocity of main air in annulus (m/s)

$V_{orifice}$: velocity of fluid through an orifice (m/s)

$V_{rim\ seal}$: velocity of air through the rim seal gap (m/s)

η: time-averaged sealing effectiveness

λ_{turb}: turbulent flow parameter, $= c_w Re_\phi^{-0.8}$

μ: dynamic viscosity of air (kg/m-s)

ρ: density (kg/m^3)

ϕ: azimuthal coordinate (°)

ϕ': nondimensionalized azimuthal coordinate, $= \phi / \Delta\phi_{vp}$

α: $V_{rim\,seal}/V_{ax}$

τ: $V_{rim\,seal}/U$

Ω: rotor disk speed

SUBSCRIPTS

1: location of static pressure measurement at 1 mm upstream of seal lip on vane platform

2: location of static pressure measurement in the disk cavity

egress: egress

ing: ingestion

purge: purge air

vp: one vane pitch

CHAPTER 1

INTRODUCTION

1.1 Background

Gas turbines use air as the working fluid and extract energy from combustion gas flow. A gas turbine is comprised of three main components: compressor, combustor and turbine (Fig. **1.1**). The incoming air is compressed before entering the combustor where it is mixed with fuel and the air-fuel mixture is ignited. Energy is extracted from the high pressure, high temperature combustion gas – a portion of which drives the compressor. Higher gas temperature at turbine inlet results in higher overall efficiency. Over the past decades, the turbine inlet temperature has risen from about 900°C to 1500°C [1]. Gas turbine operation at such high temperature, which may be well above the melting point of turbine component material, has been possible due to effective internal cooling systems.
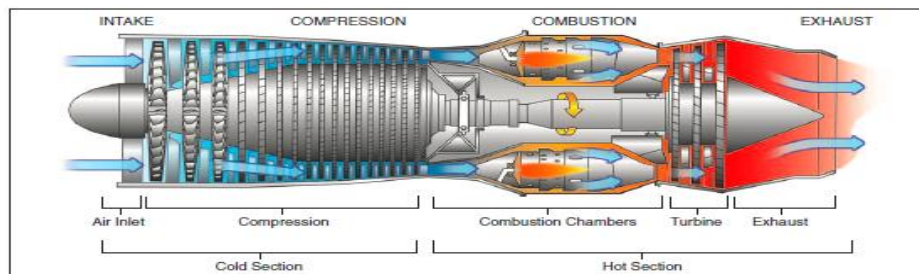
Fig. **1.1** Main Components of a Gas Turbine [2]

Figure **1.2** represents the internal secondary air system of a hypothetical gas turbine. The high-temperature gas exiting from the combustion chamber flows

over vanes and blades in the turbine section and may get transported into the wheelspace (disk cavity) between rotor and stator; this phenomenon is termed 'ingestion'. This ingestion may lead to overheating of turbine internals, especially the rotor, and reduction in its durability. Ingestion of hot gas from the main annulus into the disk cavity can be rotationally driven as well as main annulus flow driven. The latter is caused by the circumferential pressure asymmetry in the annulus and is the dominant mechanism of ingestion at engine operating condition.

Ingestion of hot main gas is typically countered by seals installed at the rim of stator and rotor and supply of secondary (purge) air bled from the compressor to the disk cavities.
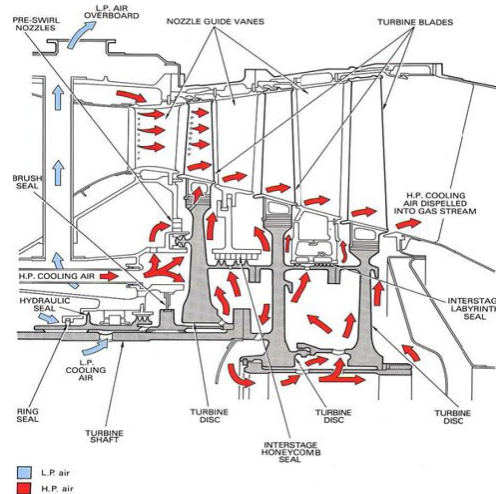
Fig. **1.2** Schematic Diagram - Gas Turbine Internal Secondary Air System
(Courtesy: The Jet Engine, 1986)

Excessive use of purge air leads to a reduction in gas turbine efficiency. On the other hand, insufficient supply of purge air leads to higher ingestion and

2

consequent overheating of the rotor. As such, an important objective of the gas turbine designer is to use the purge air optimally. To estimate the minimum purge flow necessary for complete sealing of disk cavity, a sound understanding of fluid dynamics in the disk cavity as well as in the main gas path is required.

1.2 Motivation and Overview of the Present Work

Experiments have been performed on a subscale single-stage axial turbine featuring vanes, blades, an axially-overlapping radial-clearance rim seal and a labyrinth seal radially inboard within the disk cavity. The most important use of subscale experiments is to obtain bench-mark quality data on basic processes to validate CFD (in-house, commercial) codes.

The description of this work is organized as follows:

Chapter 1:   briefly explains the role of gas turbine in an air-breathing engine and addresses the problem of ingestion which forms the basis of the present work.

Chapter 2:   provides a brief discussion of the fluid dynamics in a rotor-stator disk cavity and cites the major contributions made in the field of ingestion research.

Chapter 3:   describes the experimental facility and the procedure of experiments.

Chapter 4:   provides detailed derivation of orifice model equations for the calculation of ingestion and egress discharge coefficients and estimation of $c_{w,min}$.

Chapter 5:   contains the experimental results and their discussion.

Chapter 6:   presents concluding remarks and provides suggestions for future research.

CHAPTER 2

LITERATURE REVIEW

Theoretical, experimental, and computational research aimed at understanding the factors that influence ingestion into rotor-stator disk cavity of gas turbine engines have been carried out for many decades. Some of the important efforts are briefly discussed in the following.

2.1 Fluid Dynamics in Rotor-Stator Disk Cavity

Without Purge Air Flow

In 1951 and '53, theories were proposed by Batchelor [5] and Stewartson [6], on the fluid flow field in a rotor-stator disk cavity. According to Batchelor, a core of fluid in the disk cavity rotates at an angular velocity between zero and the rotational speed of rotor disk, Ω; also boundary layers exist on both rotor and stator surfaces.

Figure **2.1(a)** shows the Batchelor model for the fluid flow. The ambient air from a quiescent environment is drawn into the disk cavity due to disk pumping effect, and flows radially inward in the stator boundary layer, from where it gets transported into the rotating core. The fluid in the rotor boundary layer is entrained from the rotating core; the flow is in radially outward direction. Another example of Batchelor flow model is shown in Fig. **2.1(b)**, for an enclosed rotor-stator disk cavity.
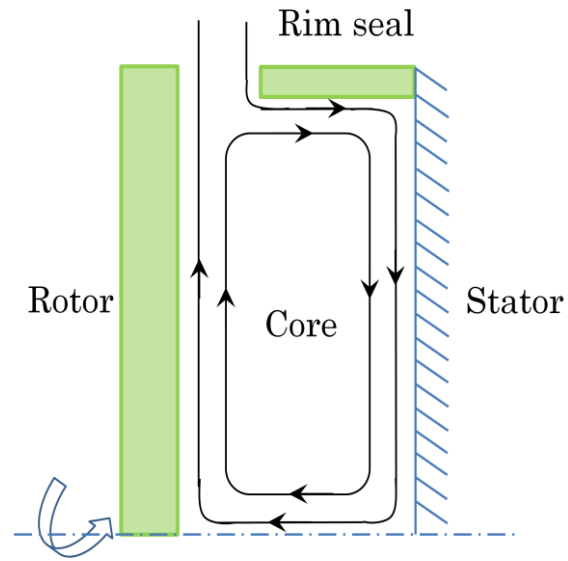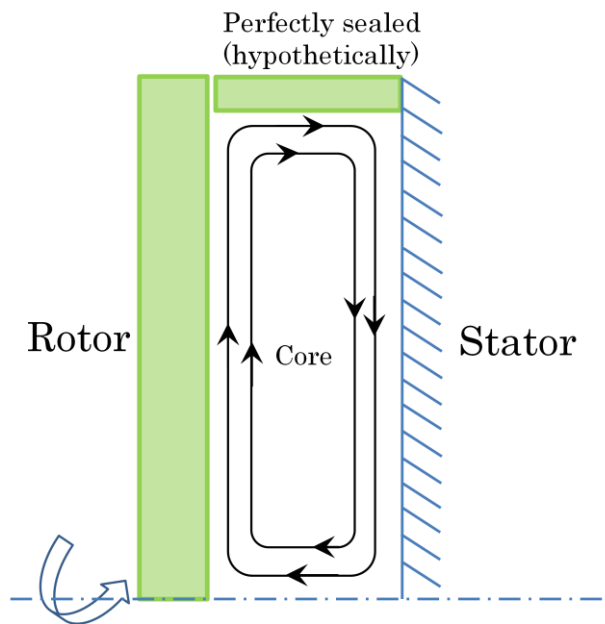
Fig. **2.1** Batchelor's Flow Model for a Rotor-Stator Disk Cavity (a) Open to Quiescent Atmosphere, (b) Completely Sealed Off From the Ambient (Enclosed Cavity)
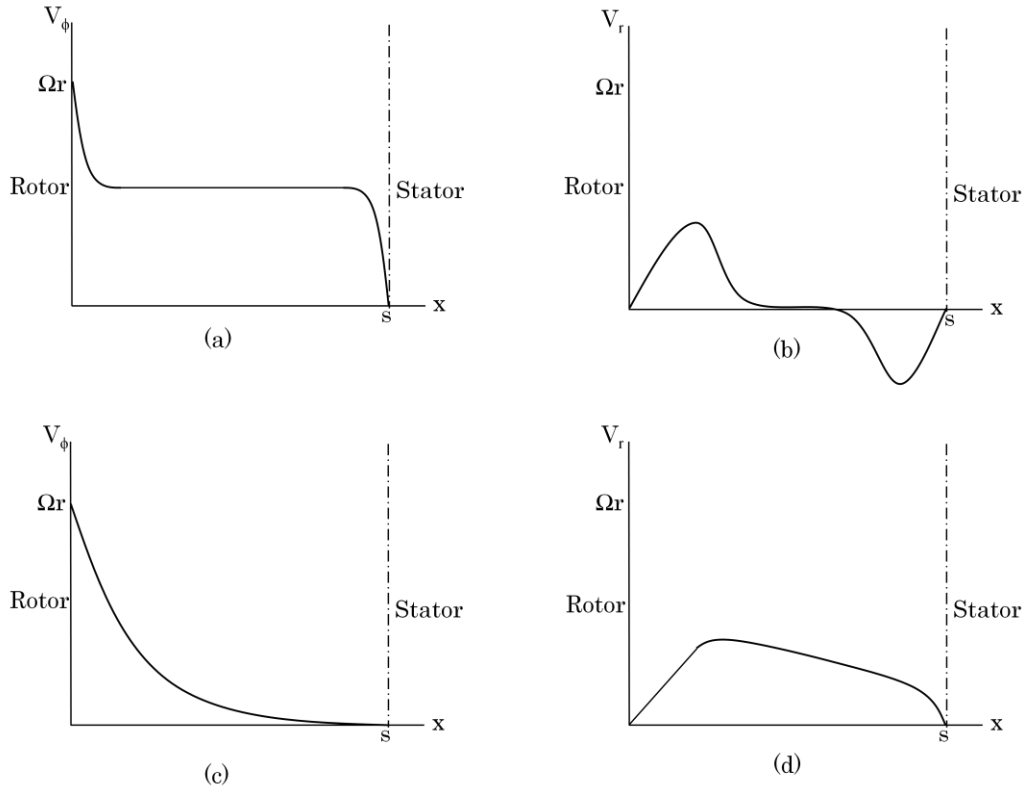
Fig. **2.2** Nondimensional Tangential and Radial Velocity Profiles in a Rotor-Stator Disk Cavity; (a) and (b): Batchelor's Model, (c) and (d): Stewartson's Model

In the Stewartson model, a boundary layer exists on the rotor surface in which the fluid tangential velocity varies from Ωr at the rotor surface to zero at locations far from the rotor. It can be seen in Fig. **2.2(a)**, that the core rotates at a uniform tangential velocity whereas Fig. **2.2(c)** implies no core rotation exists between rotor and stator. On the other hand, in Fig. **2.2(b)**, negative radial velocities in stator boundary layer indicates ingestion of air from the ambient into the disk cavity, whereas Fig. **2.2(c)**, **(d)** indicate negligible (or very low)

tangential and radial fluid velocities near the stator surface; thus no boundary layer exists near the stator surface according to Stewartson flow model.

It has been shown later experimentally that the fluid flow field in such a rotor-stator disk cavity (Fig. 2.1(a)) conforms to the Batchelor model; the Stewartson model is valid only for the rotation of a free disk in a quiescent environment.

Daily and Nece (1960) [7] conducted experiments in an enclosed rotor-stator disk cavity and identified four flow regimes based on the gap ratio ($G = s/R_h$) and rotational Reynolds number (Re_ϕ). Figure 2.3 shows the four different flow regimes:

Regime [1]:   Laminar flow for small gap ratio; merged boundary layers

Regime [2]:   Laminar flow for large gap ratio; when the axial gap is greater than the collective thickness of boundary layers on rotor and stator

Regime [3]:   Turbulent flow for small gap ratio; for higher Re_ϕ, the flow in the small space between rotor and stator becomes turbulent; merged boundary layers

Regime [4]:   Turbulent flow for large gap ratio; separate rotor and stator boundary layers

With Purge Air Flow

The supply of purge air to a disk cavity implies that the net radial flow from the cavity is radially outward. However, this does not imply that all of the flow is radially outward. If the disk pumping flow rate is greater than the purge air flow rate, the fluid in the external environment will be drawn into the disk cavity to satisfy the continuity equation:

$$\dot{m}_{in} - \dot{m}_{out} = 0 \qquad (2.1)$$

$$\dot{m}_{ing} + \dot{m}_{purge} = \dot{m}_{egress} \qquad (2.2)$$
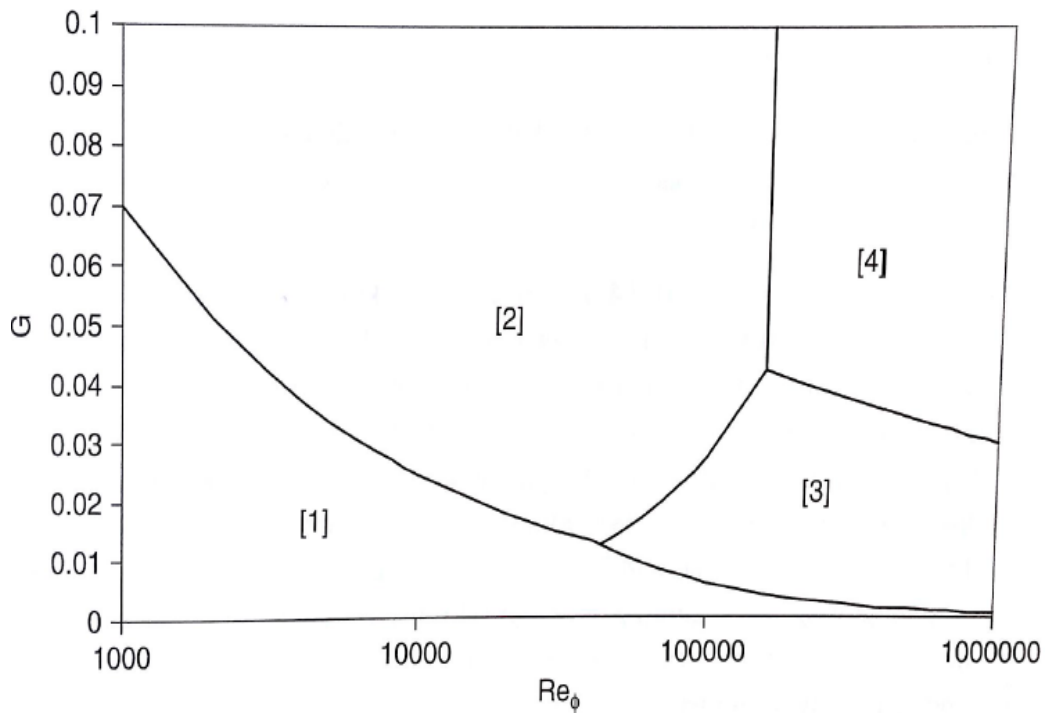
Fig. **2.3** Flow Regimes Proposed by Daily and Nece – Image Source: P.R.N. Childs [8]

9

Note that all the terms in Eq. **2.2** will have positive values. A qualitative representation of flow inside a disk cavity with an axially-overlapping radial-clearance seal is shown in Fig. **2.4.**
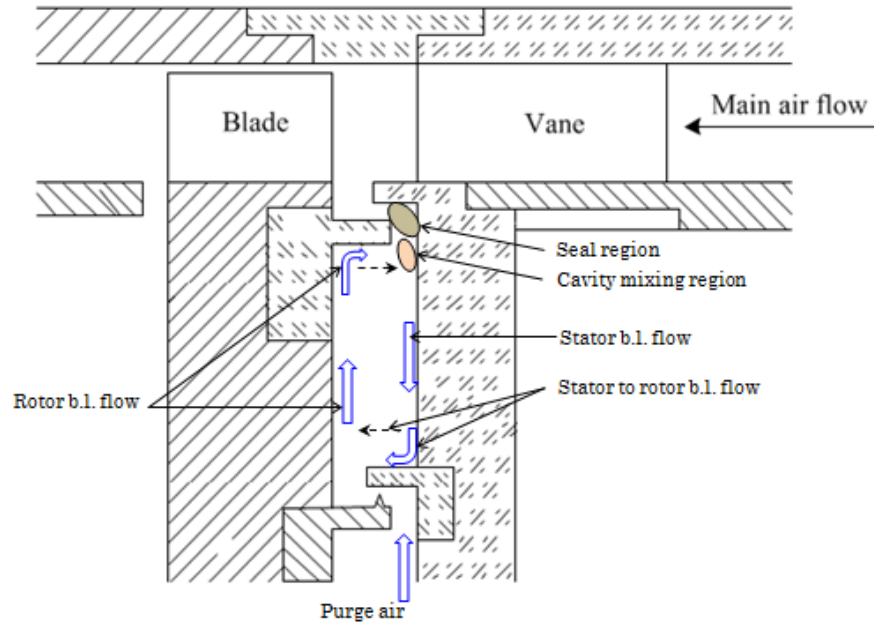
Fig. **2.4** Schematic of Flow Inside a Rotor-Stator Disk Cavity With an Axially-overlapping Radial-clearance Rim Seal With Representation of Seal and Mixing Regions [9]

2.2 Ingestion into Disk Cavity

Bailey and Owen [10, 11] were among the first to address the problem of rim seal ingestion into the disk cavity. They studied the effect of disk-pumping on the fluid flow in a shrouded disk system (quiescent environment, vanes and blades absent) with a radial outflow of purge air [11]. The equation of motion for an inviscid core of fluid rotating in the cavity was used:

$$-\frac{1}{\rho}\frac{dp}{dr} = V_r \frac{\partial V_r}{\partial r} - \frac{V_\phi{}^2}{r} \tag{2.3}$$

Equation **2.3** was integrated from a radial position within the disk cavity to its outer radius to obtain the following equation,

$$\Delta C_p = Ac_w{}^2 - BRe_\phi{}^2 \qquad\qquad (\textbf{2.4})$$

where, ΔC_p is a non-dimensional quantity representing the pressure differential between the external environment and a location in the cavity. The authors stated that $\Delta C_p = 0$ implies 'zero ingestion'. Using this concept and Eq. **2.4**, the following correlation was proposed; it was widely accepted:

$$c_{w,min} = 0.61G_cRe_\phi \qquad\qquad (\textbf{2.5})$$

Phadke and Owen published a series of three papers [**12-14**] which described experiments conducted with seven different rim seal geometries (no vanes and blades) under different external conditions, viz., quiescent environment [**12**], quasi-axisymmetric [**13**] and non-axisymmetric [**13**] circumferential pressure distribution in main annulus.

In part-I [**12**], flow visualization, pressure measurement and concentration measurement were used to study the mechanism of ingestion into the rim cavity and to find the dependence of $c_{w,min}$ on G_c and Re_ϕ. It was concluded that the rim seal configurations could be ranked on the basis of $c_{w,min}$. For any given Re_ϕ, $c_{w,min}$ was higher for higher values of gap ratios; $c_{w,min}$ was found to be proportional to Re_ϕ for any particular gap ratio.

In part-II [13], the flow in the annulus was called 'quasi-axisymmetric' as some asymmetry was observed because of misalignment in the annulus. The authors identified two flow regimes - rotationally dominated ingress (RI) [38] and external flow dominated ingress (EI) [35]. RI ingress was observed at low values of Re_{R_h}/Re_ϕ ($c_{w,min}$ decreased with Re_{R_h}) and EI ingress was observed at high values of Re_{R_h}/Re_ϕ ($c_{w,min}$ increased with Re_{R_h}), Fig. **2.5**.

In part-III [14], for external flow dominated regime, $c_{w,min}$ was related to the circumferential pressure asymmetry in the main gas annulus (P_{max}):

$$c_{w,min} = 2\pi K G_c P_{max}{}^{0.5} \qquad\qquad (\mathbf{2.6})$$

where, $P_{max} = \frac{\rho \Delta p_{max} R_h{}^2}{\mu^2}$, Δp_{max} : being the difference between the maximum and minimum pressures measured at 27 circumferential locations spread over 360°. For four different rim seal configurations, $c_{w,min}$ was plotted versus $2\pi G_c P_{max}{}^{0.5}$ (Fig. **2.6**), and a linear-fit was obtained adopting K = 0.6.

For given main air and purge air flow rates, ingestion through different rim seal configurations will be different; more complex the flow path near the rim seal, the lower will be $c_{w,min}$ [15, 16].

Ko [17] investigated the flow in a rotor-stator cavity at engine conditions, by numerically solving the elliptic form of Reynolds-Averaged Navier Stokes (RANS) equation for compressible turbulent flow. The gap recirculation zone (GRZ) formed below the shroud axial gap was considered to be the main cause of
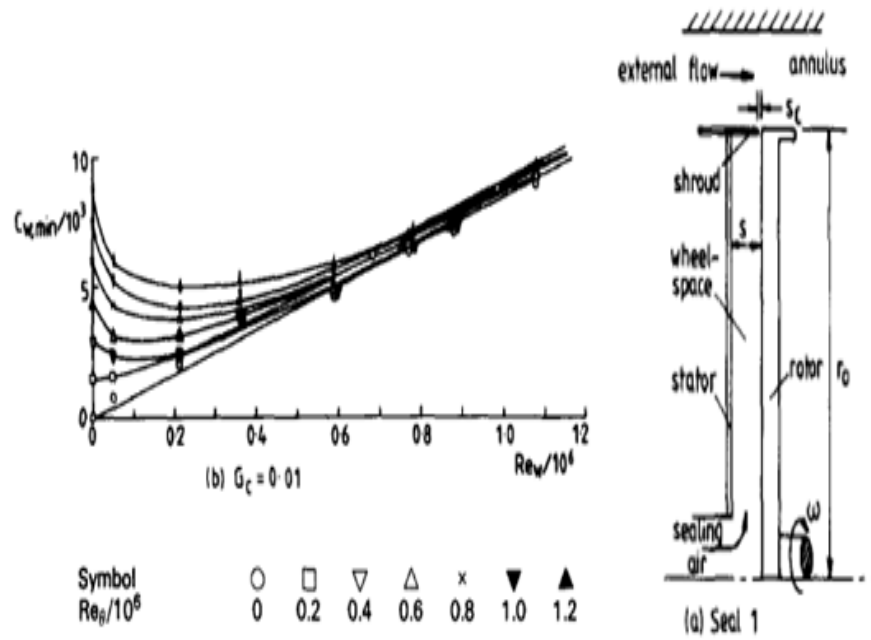
Fig. **2.5** Dependence of $c_{w,min}$ on Re_{ϕ} ($\equiv Re_{\theta}$) and Re_{R_h} ($\equiv Re_w$) [13]
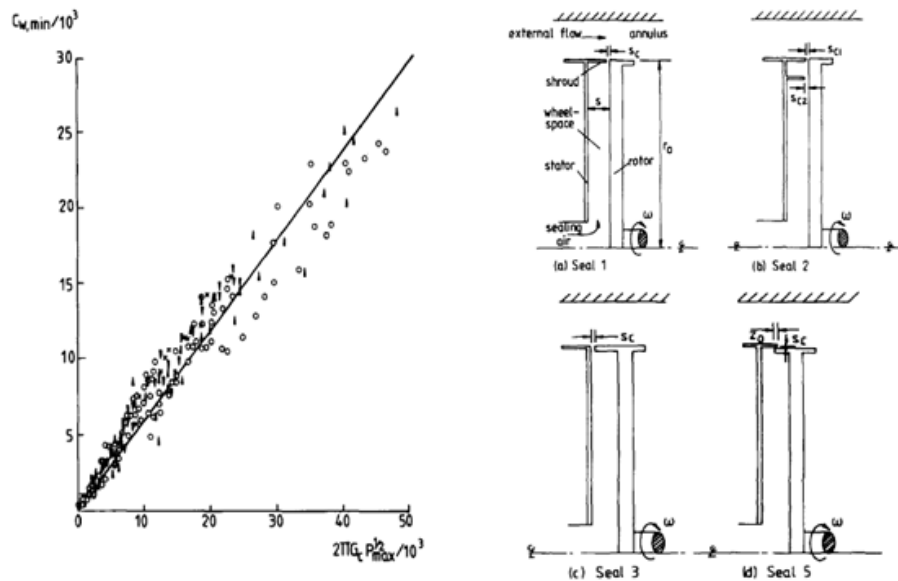
Fig. **2.6** Linear-Fit for Different Values of $c_{w,min}$ for Four Rim Seal Configurations [14]

13

(i) transport of thermal energy from the main flow to the turbine blade root and (ii) the large cavity recirculation zone formed in the disk cavity.

Daniels et. al [18] examined four different rim seal configurations, viz. axial gap, radial gap (with axial overlap - 2 configurations) and radial gap (without axial overlap). Ingestion of mainstream gas, being a mass transfer process was investigated using mass transfer analogy [42]. This analogy states that for a turbulent flow of a constant property fluid, the mass transfer equation can be changed to heat transfer equation, if the turbulent Schmidt number is equal to the turbulent Prandtl number in the velocity field. The above approximation was considered reasonable for the case where molecular weight of trace element used was close to that of the main flow. The four rim seal configurations were examined using this analogy and the authors observed that the swirl level of the flow above the rim seal had very little influence on ingestion; also decreasing the seal radial clearance resulted in better sealing than increasing the axial overlap.

Chew et. al [19] examined an axial-clearance rim seal and two radial-clearance rim seals in the absence of external flow in a study of rotationally-dominated ingestion. A mathematical model [20] developed earlier was used to obtain $c_{w,min}$; the results compared well with their experiments. However for axial-clearance rim seals with lower values of G_c, significant deviations were observed between their results and those published by Phadke et. al [15].

Chew et. al [21] carried out experiments in a model single-stage axial turbine featuring vanes and axial-clearance rim seal. CFD simulation was also

performed in which the vanes were not modeled; the flow condition near the rim seal was matched to the experiments by adjusting the inlet condition using an approximate analytical solution for a potential flow having periodic circumferential pressure variation. At higher purge air flow rates, the CFD simulations failed to replicate the extent of ingestion measured in experiments; a more detailed modeling of the main annulus flow was recommended. Discharge coefficient values were reported for a range of purge air flow rates for the case with no disk rotation and no vanes.

Johnson et. al [22] provided a list of factors responsible for mainstream gas ingestion based on the then available literature. The mechanisms were - a) disk pumping, b) circumferentially periodic vane/blade pressure field, c) existing asymmetries in the rim seal geometry, d) turbulent transport in the platform/outer cavity region, e) flow entrainment, and f) time-dependent flow structures within the cavity.

Bayley and Childs [23] used Eq. 2.3 to understand the flow within the disk cavity of a turbine stage with axial-clearance seal, as well as to predict the ingestion rates for externally and rotationally induced ingestion. The critical parameters for ingestion were: a) tangential velocity fraction ($V_\phi/\Omega r$), b) ingestion discharge coefficient, and c) egress discharge coefficient. The discharge coefficients were found using others' experimental data. The ingestion discharge coefficient was found to be strongly dependent on the purge air flow rate whereas the egress discharge coefficient did not vary much with the purge air flow rate.

15

Hills et. al [24] developed an orifice model of ingestion due to pressure asymmetries in the main gas flow annulus assuming that the length scale for circumferential variation in the main gas path is much greater than the seal clearance, so that the flow across the seal can be treated as locally two-dimensional. This model was used at locations over the circumference and the overall inflow and outflow rates of air were obtained by integration. The authors conducted experiments on a single-stage axial turbine with vanes and rotor with aluminum pegs (representing blades) attached to its periphery. A commercial CFD code, FLUENT5, was used to solve compressible, 3D, unsteady, RANS equations. The main factors identified for ingestion were: a) the unsteadiness in the main gas path created by the pegs, and b) swirl in the main gas annulus. The conclusion of Hills et. al, that the ingestion into the disk cavity depends on the unsteadiness in the main gas flow conforms to an earlier study conducted by Roy et. al at Arizona State University [25].

Roy et. al [25] performed experiments in a model single-stage axial turbine featuring vanes and blades to measure time-averaged and unsteady pressure fields. It was found that 3D steady simulations failed to predict ingestion at conditions where ingestion was found by tracer gas concentration measurements. The authors concluded that the unsteady pressure field due to vane-blade interaction was one of the reasons for main gas ingestion [25, 26]. A 3D unsteady simulation was recommended for accurate prediction of ingestion.

16

Roy et. al [27-32] examined various rim seal configurations using experimental methods such as, PIV, tracer gas concentration measurement, time-averaged static pressure measurement, and unsteady pressure measurement. The objectives were to study the flow field in the rotor-stator disk cavity, interaction of cavity egress flow with the main flow, characterization of ingestion through rim seal for a range of purge air flow rate.

Gentilhomme et. al [33] conducted experiments on a model single-stage axial turbine featuring vanes, blades, and a radial-clearance rim seal with axial overlap. CFD simulations were also carried out (without purge air flow) for three cases: a) with vanes and no blades, b) with blades and no vanes, and c) with vanes and blades. It was found that the k-ε turbulence model overpredicted the pressure asymmetry amplitude whereas the Spalart-Allmaras model provided satisfactory results. The pressure asymmetry levels obtained from CFD simulations were compared with the experiments, and then used in the 'ingestion model' developed by Hills et. al [24]. The authors concluded that at lower purge air flow rates, the ingestion of main annulus air leads to increased level of swirl in the rim cavity resulting in high pressure gradients in the cavity.

Bohn et. al [34] carried out experiments on a 1.5-stage model axial turbine equipped with vanes and blades and examined two rim seal configurations, viz. axial clearance seal and axially-overlapping radial clearance seal. It was observed that in the case of axial seal clearance, the guide vanes influenced the flow field in the rim seal gap as well as in the rim cavity, whereas for radial clearance seal, the

17

influence of guide vanes was restricted to the rim seal gap alone. The radial clearance seal with axial overlap had higher sealing performance than the axial clearance seal.

Johnson et. al [9] developed an extended rim seal orifice model in which the difference between the pressure near the lip of the seal and a 'disk cavity pressure' was considered to be the driving potential for ingestion and egress. This was the first time when two different discharge coefficients, for ingestion and egress, were proposed. The values of ingestion and egress discharge coefficients were estimated for an axially-overlapping radial clearance rim seal in a subscale axial turbine stage at ASU.

Sangan et. al [35] performed experiments in a model axial turbine stage for two rim seal configurations, viz. axially-overlapping radial-clearance seal and an axial-clearance seal. Sealing effectiveness, $c_{w,min}$ for externally induced (EI) ingestion and the ratio of discharge coefficient were combined in a single equation obtained from an orifice model developed at University of Bath which was first presented by Owen [36]. The orifice model effectiveness equation features two parameters, Γ_c and ϕ_{min}. A maximum likelihood estimation method [37] was used to fit model to the sealing effectiveness values obtained from experiments. This parameter estimation method provides the two unknowns Γ_c and ϕ_{min}. It was pointed out that the accuracy of these parameters increased and the variability decreased as the number of data points increased, and Γ_c and ϕ_{min} were in close agreement to the *'true values'* (the theoretical curve being the *'true curve'* and the

then obtained values of Γ_c and ϕ_{min} from the orifice model effectiveness equation are called *'true values'*) for all $n \geq 16$. Ingestion and egress discharge coefficients could be subsequently determined using the peak-to-trough pressure differential in the main gas annulus measured at zero purge air flow rate.

This work was extended for rotationally induced (RI) ingestion by Sangan et. al [38]. Experiments were carried out in a turbine stage featuring vanes and blades, where the inlet to the annulus was closed off while the outlet was open to atmosphere. Thus, the swirl created in the external fluid was only due to the disk rotation. Their same orifice model [36] was modified for RI ingestion, and sealing effectiveness, $(c_{w,min})_{RI}$ and $\Gamma_c(= C_{di}/C_{de})$ were combined in one orifice model sealing effectiveness equation. The value of $(c_{w,min})_{RI}$ obtained for the axial-clearance seal was found to be independent of rotational Reynolds number.

CHAPTER 3

EXPERIMENTS

3.1 Experimental Facility

The experimental facility is shown in Fig. **3.1**. It is an open air facility where laboratory ambient air is drawn into the test rig by the centrifugal main blower (operating in suction mode) and discharged into the atmosphere via a vertical circular duct. The secondary blower also draws air from the laboratory ambient and the secondary air is supplied to the disk cavity via a tube. Figure **3.2** shows the schematic of the test rig on which earlier research work by Roy et. al [9, 25-32] were carried out.
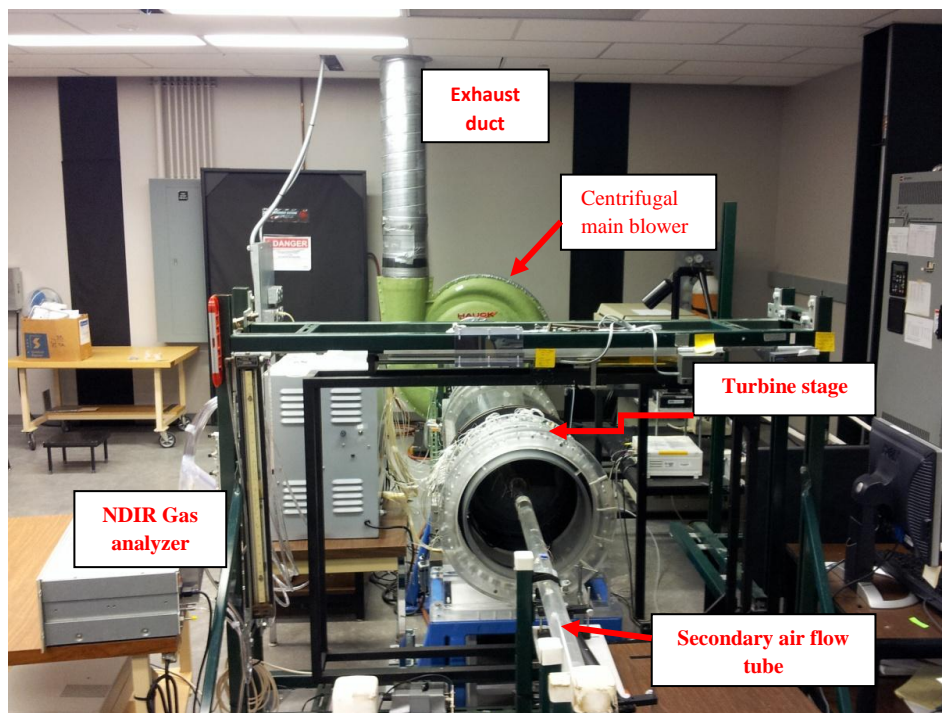
Fig. **3.1** The Experimental Facility

Experiments by Thiagarajan [39] and Pathak [40] were carried on the current turbine stage; some geometrical modifications (e.g., the labyrinth seal clearance) were introduced in the present study.
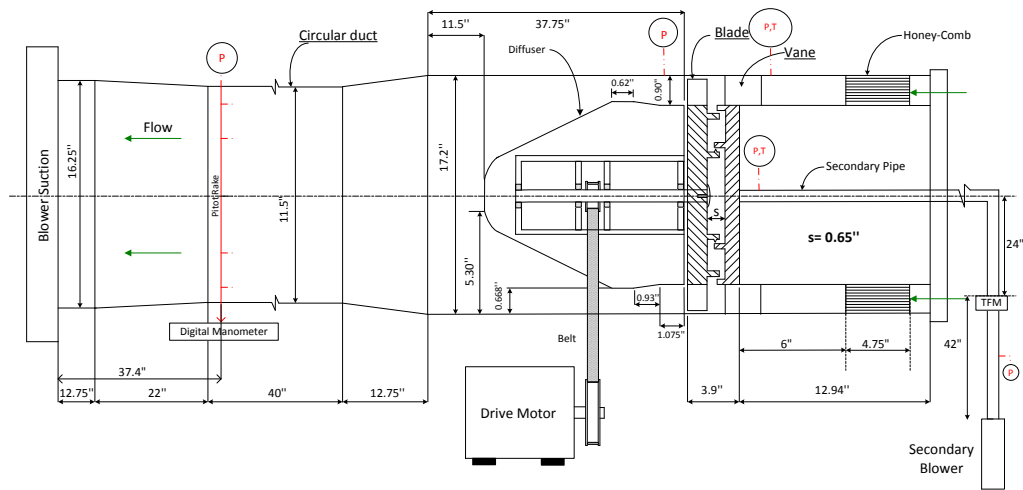
Fig. **3.2** Schematic of the Test Rig

Centrifugal Main Blower

The test rig is situated on the suction side of the centrifugal blower (22.4 kW, HAUCK, TBA-20-30). The centrifugal blower can draw air upto 1.42 m^3/s ($\approx$3000 cfm). The blower motor is controlled by a Cutler-Hammer Variable-Frequency Drive (AF-9) rated at 75 HP. The blower inlet has a diameter of 412.7 mm (16.25") and is connected to a diffuser section (angle of divergence = 5°) which in turn is connected to a plexiglass circular duct of inlet diameter 292.1 mm (11.5"), Fig. **3.2**. The main air is discharged to the atmosphere through 2.23 m (7'4") long vertical pipe of 311 mm (12.25") inner diameter that connects to an exhaust duct on the building roof.

21

Centrifugal Secondary Blower

The secondary (purge) air is provided by a centrifugal blower (2.24 kW, HAUCK, TBA-16-3), which is controlled by a variable-frequency drive (Emerson, Prism, rated at 4.84 kW). The blower can draw air upto 0.12 m^3/s ($\approx$ 250 cfm). The blower discharge is connected to a 1.67 m (5'6") long, 50.8 mm (2") diameter GI pipe on which a turbine flowmeter has been installed at a distance of 1.07 m (3'6") from the blower discharge.

Purge Air Flow Path

The purge air flow rate is measured by a turbine flowmeter (EG&G Technologies) with an uncertainty of ±0.2% of the displayed value. Sufficient length (L/d $\approx$ 21) was provided for the flow to become fully developed before reaching the turbine flowmeter. A 90° ball valve is located 0.6 m (24") downstream of the turbine flowmeter; two 45° elbows align the 1.78 m (5'10") long purge flow tube with the centerline of the stator. To straighten the incoming air flow, a honeycomb mesh (12.7 mm (0.5") long, 3.2 mm (0.126") hexagonal cell size) has been installed in the 1.78 m (5'10") long purge air flow tube.

Main Air Flow Rate Measurement

A pitot tube rake comprising of five pitot-static tubes (United Sensor, UNSH-N-107) has been installed at $\approx$ 2.23 m (7'4"), Fig. **3.2**, downstream of the turbine stage in a circular pipe of 292.1 mm (11.5") inner diameter. The rake manifold along with a static pressure tap are connected to a digital manometer

(Validyne: PS309) which measures the dynamic head of the air flowing in the duct.

$$P_{stagnation} = P_{static} + P_{dynamic} \qquad \qquad (\mathbf{3.1})$$

$$P_{dynamic} = P_{stagnation} - P_{static} = 0.5\rho v^2 \qquad \qquad (\mathbf{3.2})$$

$$\text{Flowrate}, Q(cfm) = 200.8 \times (P_{dynamic}/\rho)^{0.5} \qquad \qquad (\mathbf{3.3})$$

where, $P_{dynamic}$ and ρ are in S.I. units.

The range of PS309 is 0-2 VDC (1 Volt = 1 inch H_2O pressure head). The accuracy of the unit is 0.25% of the full scale reading. PS309 also provides an analog output which is routed to the DATA6500 via a BNC cable. The DATA6500 is programmed so as to display the mean and RMS values of main air flow rate based on 1024 data points with a sampling period of 0.1 s.

3.1.1 Turbine Stage

The turbine stage is shown schematically in Fig. **3.3**. The main air from the laboratory ambient enters the turbine stage via a 120.7 mm (4.75") long honeycomb section (Polypropylene, 0.315" cell size, black, Plascore, PP30-5) installed 152.4 mm (6") upstream of the stator vanes leading edge plane.

The Rotor

The aluminum rotor has a diameter of 391.4 mm (15.41"). It is equipped with 28 partial-height, partial-length blades, Figs. **3.3** and **3.4**. The blade tip clearance from the steel outer shroud is 1.5 mm (0.059").

The Rotor Drive System

The rotor is mounted on a 50.8 mm (2") diameter mild-steel shaft on which a 22 - teeth pulley has also been mounted; the pulley is rotated by a belt which connects to a 72 - teeth pulley installed on a shaft connected to motor (3HP, maximum speed: 1750 rpm). The pulley teeth ratio of 3.27 allows a maximum rotor speed of 5722 rpm. The motor is controlled by a 5 HP Eaton-Cutler Hammer Adjustable Frequency Drive (AFD).

The rotational speed of the motor shaft is measured using a digital photoelectric tachometer (Biddle Instruments, accuracy ±1rpm). When the test rig is operational, the motor acts as generator because of the energy input from the main air flow. The excess energy is transferred to a capacitor in the AFD. A current flows from the capacitor to a braking resistor where the excess energy is dissipated as heat. The braking resistor is a bank of 7 resistors connected in series (65Ω total). It is rated at 2.7 kW with a 50% duty-cycle.
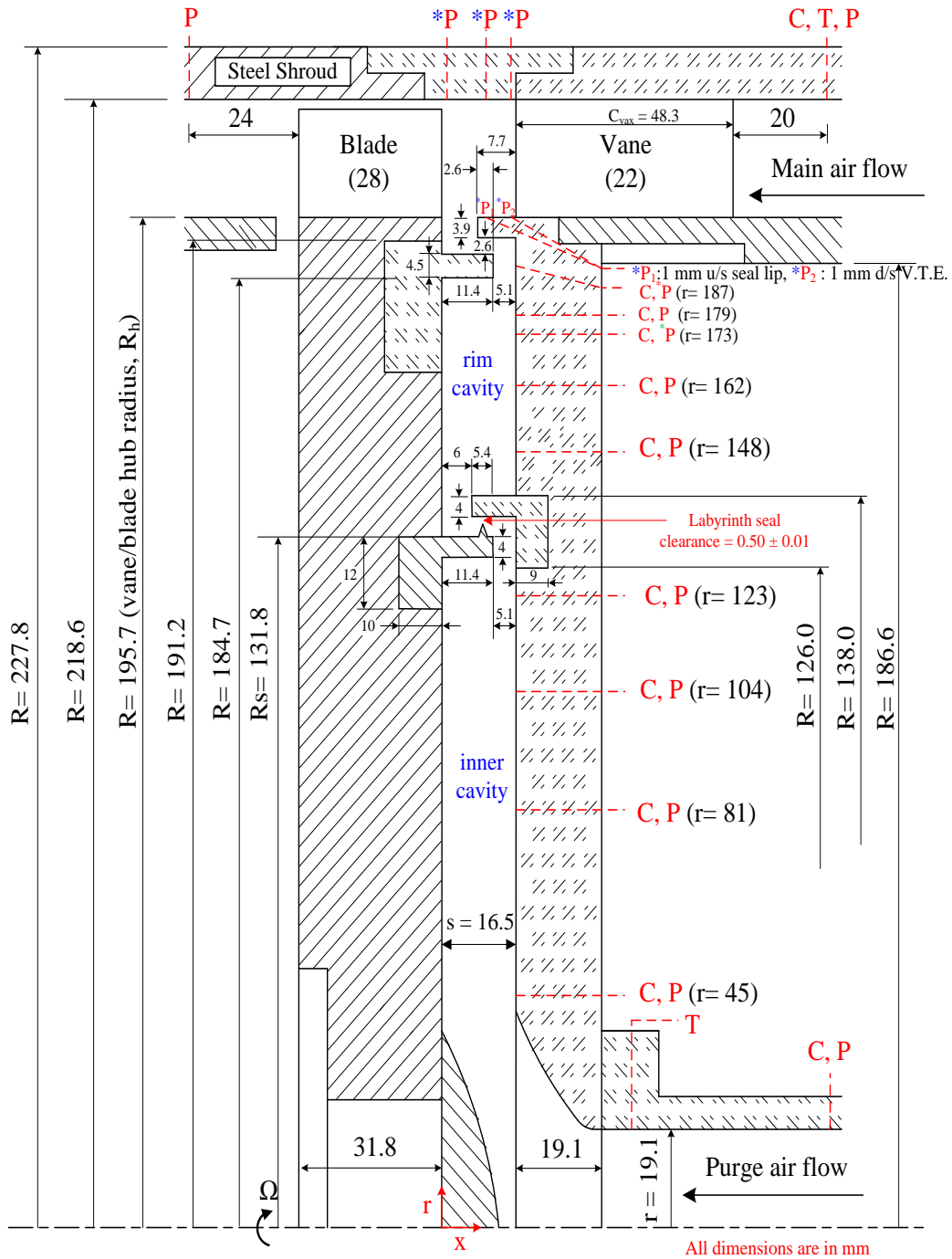
Fig. **3.3** Schematic of the Single-Stage Subscale Axial Turbine (C: Concentration Tap on the Stator Surface; P: Pressure Tap; T: Thermocouple)

The Stator

The plexiglass stator has a diameter of 391.4 mm (15.41") and thickness of 19.05 mm (0.75"). It is equipped with 22 partial-height, full length vanes. The vane profile imparts swirl to the incoming flow, turning it by an angle of 68.6°. For a given main blower operating condition, the partial vane height allows a sufficiently high main air axial velocity in the annulus that results in an acceptable velocity triangle upstream of the blade row at prescribed rotor speeds. Figure **3.4** shows the vane and blade arrangement and the resulting velocity triangles. The velocity triangles shown are assumed to be undisturbed by the secondary flow as the maximum ratio of purge air flow rate to main air flow rate is very small.

Rotor-stator Disk Cavity

The disk cavity is divided into rim cavity and inner cavity by a labyrinth seal (Fig. **3.3**). The labyrinth seal has a single tooth; the part on the rotor extends radially from 127.8 mm to 131.8 mm while the part of the seal on stator extends radially from 134 mm to 138 mm. This seal provides a radial clearance of 0.5 mm ±0.01 mm at the tooth and an axial overlap of 5.4 mm.

The part of the rim seal on the rotor extends radially from 184.7 mm to 189.2 mm; the part on the stator extends radially from 191.8 mm to the hub radius (R_h = 195.7 mm). The rim seal has a radial clearance of 2.6 mm and an axial overlap of 2.6 mm.

The axial gap between the stator surface and the rotor surface is 16.5 mm.
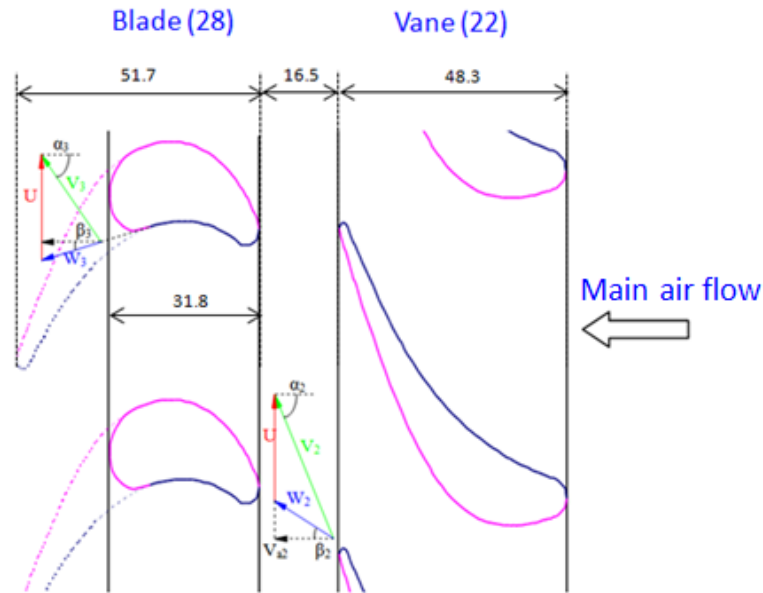
Fig. **3.4** Velocity Triangles Downstream of Vanes and Downstream of Blades

3.1.2 Pressure and Ingestion Measurements

Static Pressure and Ingestion Measurement Locations

The turbine stage drawing (Fig. **3.3**) shows the locations where time-averaged static pressure and time-averaged ingestion were measured. In the inner cavity, static pressure is measured at four radial locations, viz. 45 mm, 81 mm, 104 mm and 123 mm. In the rim cavity, static pressure is measured at five radial locations, viz. 148 mm, 162 mm, 173 mm, 179 mm and 187 mm. The pressure tap circumferential locations in the main gas path at the outer shroud and at the vane platform are indicated in Figs. **3.5** and **3.6** respectively. At the radial location 173 mm, pressure is measured at six circumferential locations spread over one vane pitch to check possible variation in the pressure distribution. At the radial location

27

187 mm, pressure is measured at 17 circumferential locations spread over one vane pitch. On the vane platform, pressure is measured at two axial locations, viz. 1 mm downstream of vane trailing edge and 1 mm upstream of rim seal lip. At both these axial locations on the vane platform, pressure is measured at 33 circumferential locations spread over two vane pitches. Static pressure is measured at three axial locations at the outer shroud: 1 mm downstream of vane trailing edge plane, 5 mm downstream of vane trailing edge plane and 1 mm upstream of blade leading edge plane. At these three axial locations, pressure is measured at 33 circumferential locations over two vane pitches. Also, pressure is measured at the main gas path outer shroud - 20 mm upstream of the vane leading edge plane and 24 mm downstream of blade trailing edge plane. These two pressures are considered to represent the inlet and exit pressures of the turbine stage.

Time-averaged volumetric concentration of the tracer gas (CO_2) is measured at the stator surface at four locations in the inner cavity and five locations in the rim cavity. The radial locations for these measurements are same as the static pressure measurement locations mentioned above. Tracer gas concentration is also measured in the purge air flow supply pipe near the disk cavity inlet.

.
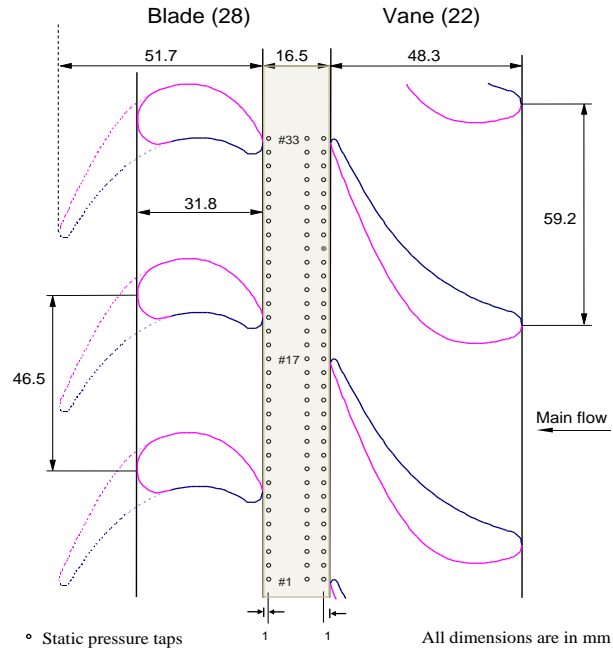
Fig. **3.5** Circumferential Locations of Static Pressure Taps on the Outer Shroud in Main Gas Flow Annulus at 1 mm Downstream of Vane Trailing Edge Plane, 5 mm Downstream of Vane Trailing Edge Plane and 1 mm Upstream of Blade Leading Edge Plane
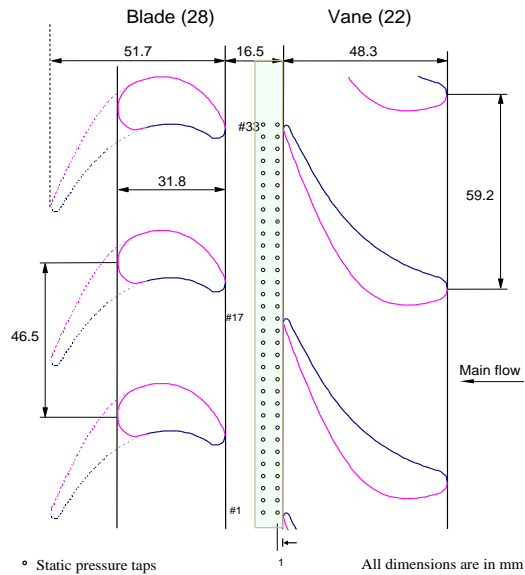
Fig. **3.6** Circumferential Locations of Static Pressure Taps on Vane Platform in Main Gas Flow Annulus at 1 mm Downstream of Vane Trailing Edge Plane and 1 mm Upstream of Seal Lip

3.2 Time-averaged Static Pressure Measurement

3.2.1 Components of Pressure Measurement System

Scanivalve

Scanivalve is a junction with 48 inlet channels and one output channel. The inlet channels are connected to pressure taps through flexible vinyl tubes (Scanivalve, 1.59 mm (0.063") i.d.). The output channel is connected to a pressure transducer. A manual control solenoid step-driver is used to switch through the 48 inlet channels sequentially; the inlet channel number at any particular time is displayed on the position display unit.

The following schematic shows the components of pressure measurement system.
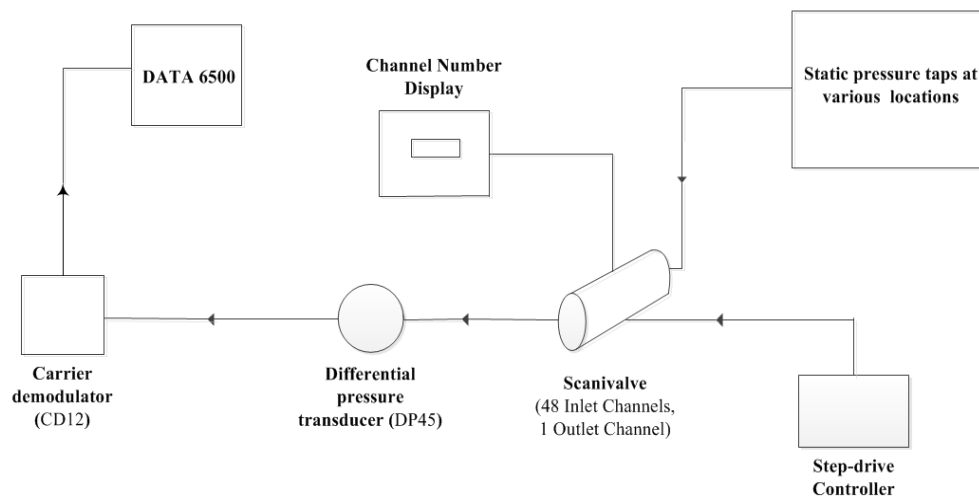
Fig. **3.7** Schematic of Components for Static Pressure Measurement

Pressure Transducer (DP45 - Validyne)

DP45 is a differential pressure transducer designed for the pressure range of 0-2 psi (0-13.79 kPa). The accuracy of DP45 is 0.5% of full scale (2 psi) and it has minimal hysteresis loss. The transducer consists of a magnetically permeable stainless steel diaphragm clamped between two blocks of stainless steel (Fig. **3.8**). At zero pressure differential, the diaphragm is at the center (zero deflection) and the distance between the diaphragm and the coil is 0.127 mm (0.005").
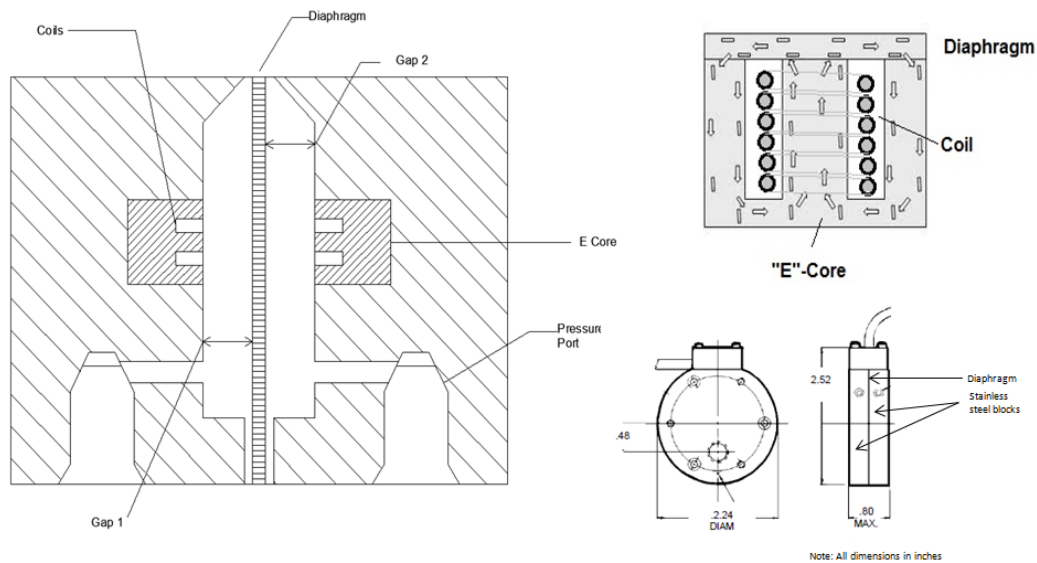
Fig. **3.8** Schematic of the Differential Pressure Transducer (DP45), Front and Side View, and E-Core

When the diaphragm is subjected to a differential pressure, it deflects towards the lower pressure cavity resulting in a different gap length. The magnetic reluctance varies with the gap length; a change in the magnetic reluctance induces a change in the induction of the coils embedded in the E core. E core laminations (made of iron) are added to the solenoid coils to direct the

magnetic field lines. Based on the change in the inductance of coils, an AC output signal linearly dependent on the pressure differential is generated. This output signal is routed to a carrier demodulator.

Carrier Demodulator (CD12 - Validyne)

The carrier demodulator (CD12) amplifies and demodulates the DP45 output. With an input sensitivity ranging from 0.9 to 75 mV/V, the CD12 converts the output of the differential pressure transducer into a DC voltage signal with a full-scale output of 10 Vdc. The carrier demodulator small deviations in the signal with respect to a reference level. It features a digital display on its front panel; its analog output is routed to the DATA6500 via a BNC cable.

Data Acquisition System (DATA6500 - Analogic)

This unit provides the mean and the RMS of the CD12 output signal. It is programmed to sample the signal at 2 kHz over a time interval of 15.36 seconds for each pressure measurement.

Static Pressure Tap (TUBN063 - Scanivalve Corp.)

Figure **3.9** shows the schematic of a stainless steel tubulation (1.59 mm (0.063") o.d.) static pressure tap. The interface between the pressure tap and plexiglass is sealed with silicone to prevent air leakage.
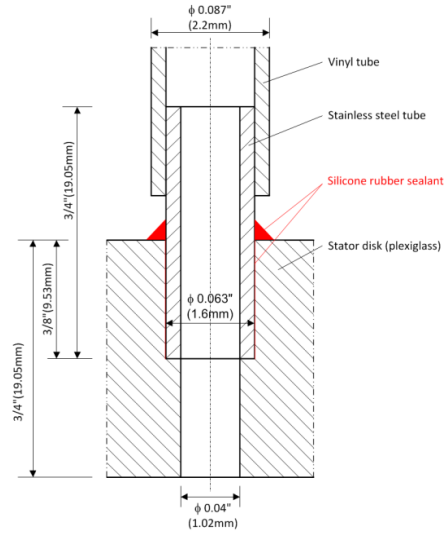
Fig. **3.9** Schematic of Pressure Tap on Stator Disk

3.2.2 Experimental Procedure for Pressure Measurement

Firstly, the main blower, secondary blower and the rotor motor are set at respective frequencies for operation of the rig at a particular experimental condition. Next, the secondary blower and the rotor motor are turned on followed by the main blower. After the main blower attains the desired rpm, the rotor motor rpm and the main air flow rate are measured via, respectively, a digital tachometer and the pitot tube-rake. Once the desired main air flow rate, secondary air flow rate and the rotor motor rpm are attained, the rig is allowed to run for about 10 minutes so that it achieves steady state. The static pressures can now be measured. The laboratory ambient pressure and temperature are monitored before the start of each experiment. The laboratory ambient pressure typically varies between 101 kPa to 102 kPa (absolute); the temperature is essentially constant at 23°C.

33

The pressure taps are connected to the Scanivalve via flexible vinyl tubings and upto 48 pressures can be measured during one run. The DATA6500 is programmed such that it displays time-averaged and rms values of static pressure for a prescribed time interval. The time-averaged static pressure is:

$$\bar{p} = \frac{1}{T} \int_{0}^{T} p(t)dt \approx \frac{1}{N} \sum_{i=1}^{N} p_i \qquad (\mathbf{3.4})$$

where, N is the number of samples collected over a time interval T.

Since the blade passage frequencies for the two experimental conditions, Table **5.1**, are 0.887 kHz and 1.12 kHz, the data are sampled at a higher frequency (2 kHz). A total of 30720 data points are collected at this sampling rate. Once the data for one pressure tap location are recorded, the Scanivalve position is changed by a manually controlled solenoid stepper motor. The maximum uncertainty in static pressure measurement is ±4% [39].

3.3 Time-averaged Mainstream Gas Ingestion Measurement

3.3.1 Components of the Ingestion Measurement System

NDIR Gas Analyzer (Ultramat23 - Siemens)

An NDIR (Non-dispersive Infrared) gas analyzer was used to measure the volumetric concentration of the tracer gas (CO_2). The gas analyzer consists of an IR measuring cell, a safety filter, flow meter and a gas pump. The tracer gas absorbs infrared radiation in a particular range of wavelength depending upon its

concentration. The radiation intensity is measured by the IR measuring cell, and the CO_2 concentration is displayed on the LCD. At the analyzer back side, ports are provided for inlet and exit of the sample gas, as well as for the inlet of the zero gas (N_2).

Tube Connections and Gas Cylinders

The ingestion measurement system is shown in Fig. **3.10**. Ultra high purity (99.9% N_2) compressed nitrogen gas was used as the zero gas for AUTOCAL. The secondary air was seeded with tracer gas (CO_2) at 1.6 m (5'3") upstream of the disk cavity entrance using a stainless steel sparger tube (6.3 mm o.d., 4.5 mm i.d.) which contains 15 holes (each of 1 mm diameter). The volumetric flow rate of tracer gas was maintained at approximately 1 liter/min by controlling the flow rate of tracer gas at the point of seeding, using a pressure regulator and a needle valve. The temperature of the tracer gas, as it flows from the cylinder, is controlled using an electric gas heater between the gas cylinder and the regulator, and a band heater at the back side of the regulator. The tracer gas temperature is measured by a J-type thermocouple and maintained close to the desired temperature.

The gas sampling taps were connected to toggle valves by vinyl tubes (0.1875" i.d., 0.3125" o.d.). The toggle valves were connected to a single-output manifold (Fig. **3.10**). A needle valve and a filter were connected to the manifold output and the sample gas was delivered to the gas analyzer via a vinyl tube.

35
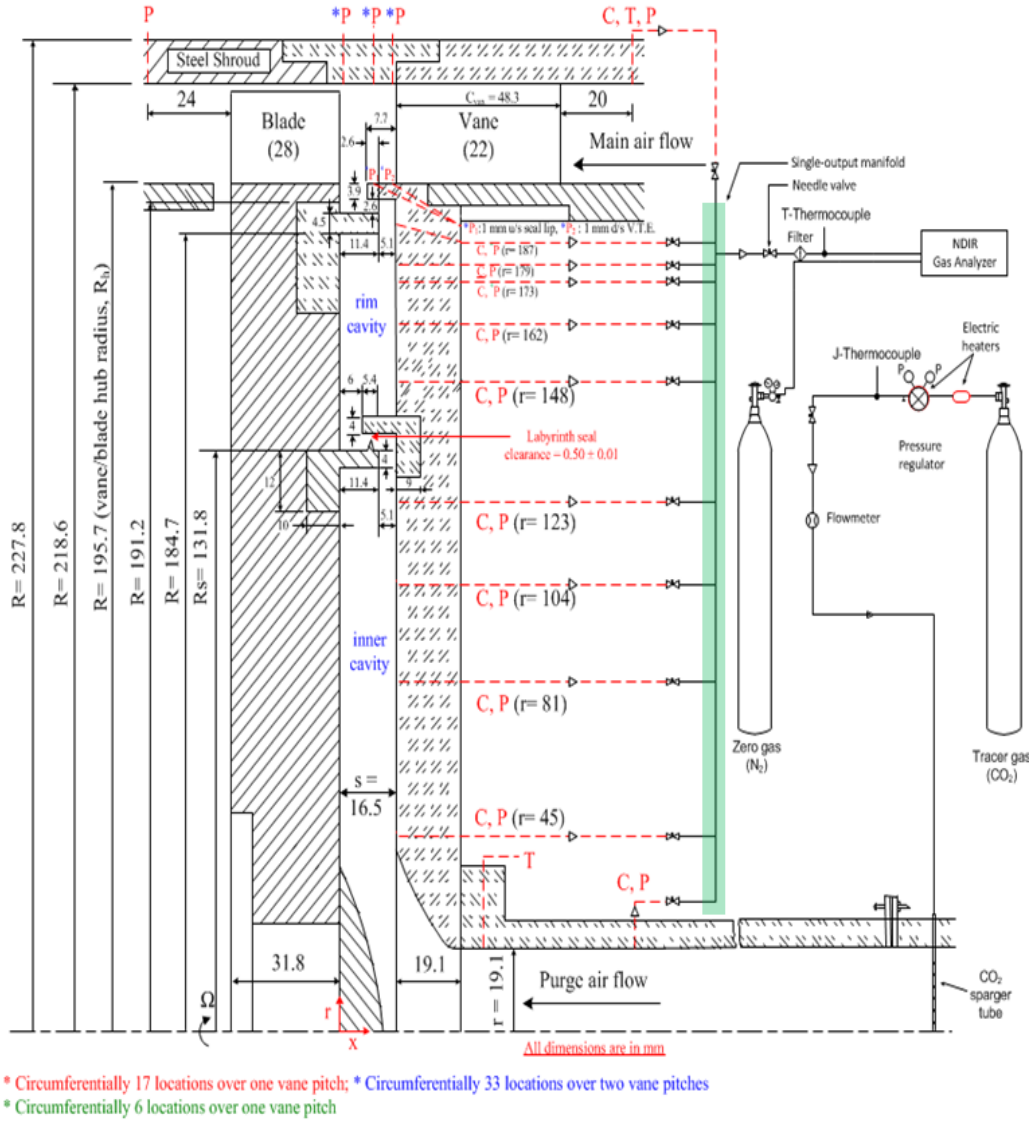
Fig. **3.10** Schematic of Ingestion Measurement System Showing the Measurement Locations, Tube Connections, Tracer Gas & Zero Gas Cylinders and their Connections

3.3.2 Experimental Procedure for Ingestion Measurements

The local sealing effectiveness, η, at r̲, is given by,

$$\eta(\underline{r}) = \frac{C(\underline{r}) - C_{main}}{C_{purge} - C_{main}}$$

(3.5)

36

where, C_{purge} is the concentration of carbon dioxide in the purge air measured at the innermost radial location (r = 45 mm) on the stator surface in the disk cavity. The volumetric concentration of CO_2 in purge air was also monitored at 0.38 m (14.96") upstream of the disk cavity entrance and always maintained at 4% by volume (5.95% by mass). The concentration at the latter location was checked multiple times during the experiments. A honeycomb mesh was installed in the secondary air flow tube to straighten the flow and help mix the carbon dioxide with the secondary air. However, the mixing of CO_2 with the purge air was found to be incomplete for the three higher purge flow rates, Table **5.1**; the 90° turn of the secondary air upon entering into the disk cavity led to better mixing. As such, the radially innermost location of measurement in the cavity (r = 45 mm) was considered to be representative of fully mixed carbon dioxide concentration in the purge air. The carbon dioxide volumetric concentration was measured at nine radial locations in the disk cavity (including the 45 mm location) utilizing the same taps that were used for the static pressure measurements. The measurement of carbon dioxide concentration takes some time; hence, it is a time-averaged value over many rotor revolutions. However, the concentrations measured are local with respect to vane position as well as to the radial positions on the stator surface. The flow of sample gas through the test cell (inside NDIR gas analyzer) is Steady State Steady Flow (SSSF). A constant flow rate of 1liter/min is maintained across the test cell; the test cell pressure (p_0) depends upon the laboratory ambient pressure and remain the same even when p_1 changes.
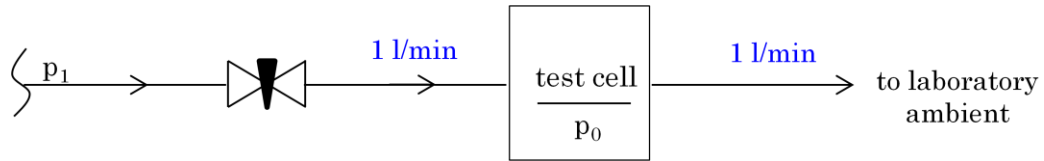
Fig. **3.11** Schematic of Sampled Gas Flow Across the Test Cell Inside NDIR Gas Analyzer

The maximum uncertainty in the tracer gas volumetric concentration measurements is ±0.11% carbon dioxide concentration (this translates to ±0.17% mass concentration) [39].

CHAPTER 4

THE ORIFICE MODEL OF INGESTION AND EGRESS

4.1 Ingestion and Egress Discharge Coefficients

The ingestion of main air from the annulus into the disk cavity is governed by a positive pressure differential between locations 1 and 2, Fig. 4.1. A negative pressure differential causes egress from the disk cavity into the main gas annulus. In the orifice model of ingestion and egress, the radial rim seal clearance (or gap) is considered as an orifice through which either ingestion or egress can occur at different azimuthal locations.
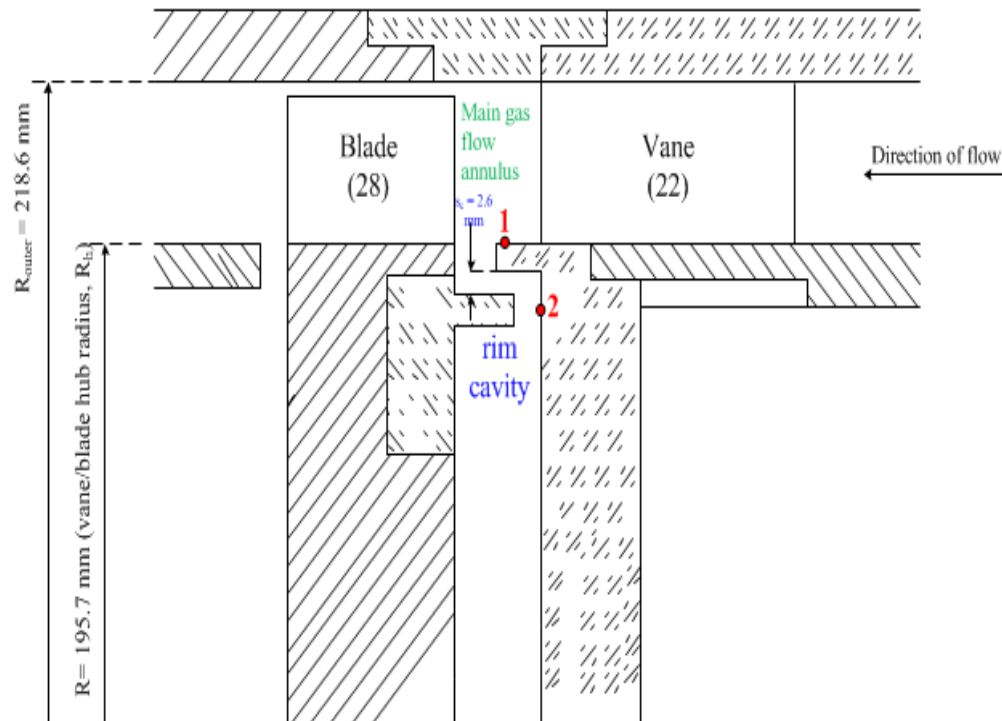
Figure 4.1 The Rim Seal Radial Clearance Considered as an Orifice, along with Locations 1 And 2 (2 is Only a Representative Location in the Rim Cavity)

The volumetric flow rate of a fluid through an orifice is given by,

$$Q_{orifice} = C_d A_{orifice} V_{orifice} \qquad (4.1)$$

$$Q_{orifice} = C_d A_{orifice} \left[\frac{2\Delta p_{orifice}}{\rho} \right]^{0.5} \qquad (4.2)$$

In terms of mass flow rate, Eq. (4.2) can be re-written as,

$$\dot{m}_{orifice} = \rho Q_{orifice} = C_d A_{orifice} [2\rho\Delta p_{orifice}]^{0.5} \qquad (4.3)$$

Since the rim seal radial gap is modeled as an orifice,

$$\dot{m}_{rim-seal} = C_d A_{gap} [2\rho\Delta p_{rim\ seal}]^{0.5}$$

The pressure differential across rim seal is:

$$\Delta p_{rim-seal} = (p_1 - p_2)$$

An appropriate location for p_2 is in the 'seal region'[9]; other locations in the rim seal cavity can be considered for parametric study. The location 1, which is 1 mm upstream of the seal lip on the vane platform, is an appropriate representative location for static pressure of the main annulus air when considering ingestion and egress.

In Fig. 4.2, the ingestion and egress region (area integrals) are,

$$\Delta a_{ing} = \int_0^{\phi_0'} (|\Delta p_{rim-seal}|)^{0.5} d\phi' \qquad (4.4a)$$

40

$$\Delta a_{\text{egress}} = \int_{\phi_0{}'}^{1} (|\Delta p_{\text{rim-seal}}|)^{0.5} d\phi' \qquad (4.4\mathbf{b})$$

where $\phi_0{}'$ is the azimuthal location where Δp changes sign.
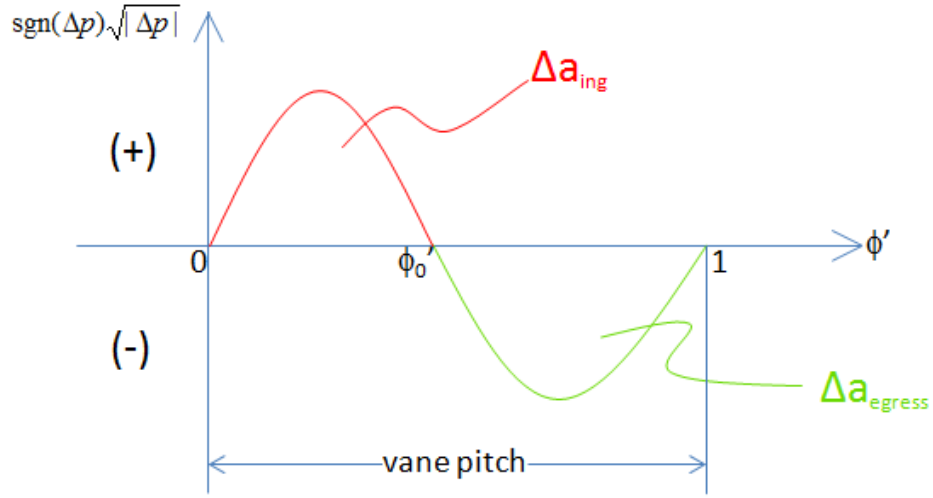
Fig. **4.2** A Schematic of Ingestion and Egress Regions Over One Vane Pitch

In Fig. **4.2**, the area integrals are given by Eqs. (**4.4a**) and (**4.4b**) are calculated by trapezoidal method of integration.

Equation (**4.3**) can be re-written as:

$$\dot{m}_{\text{ing}} = C_{\text{di}} A_{\text{gap}} \Delta a_{\text{ing}} (2\rho)^{0.5} \qquad (4.5\mathbf{a})$$

$$\dot{m}_{\text{egress}} = C_{\text{de}} A_{\text{gap}} \Delta a_{\text{egress}} (2\rho)^{0.5} \qquad (4.5\mathbf{b})$$

The sealing effectiveness, η, at location 2 is given by,

$$\eta = \frac{\dot{m}_{\text{purge}}}{\dot{m}_{\text{purge}} + \dot{m}_{\text{ing}}} = \frac{\dot{m}_{\text{purge}}}{\dot{m}_{\text{egress}}} \qquad (4.6)$$

41

$$\dot{m}_{ing} = \left(\frac{1}{\eta} - 1\right)\dot{m}_{purge} \qquad (4.7a)$$

$$\dot{m}_{egress} = \frac{\dot{m}_{purge}}{\eta} \qquad (4.7b)$$

Substituting Eqs. (4.7a) and (4.7b) in Eqs. (4.5a) and (4.5b) respectively, the ingestion and egress discharge coefficients are given by,

$$C_{di} = \left(\frac{1}{\eta} - 1\right)\frac{\dot{m}_{purge}}{\Delta a_{ing}A_{gap}(2\rho)^{0.5}} \qquad (4.8a)$$

$$C_{de} = \left(\frac{1}{\eta}\right)\frac{\dot{m}_{purge}}{\Delta a_{egress}A_{gap}(2\rho)^{0.5}} \qquad (4.8b)$$

4.2 Estimation of the Minimum Sealing Flow Required

For both set of experiments, $\dot{m}_{ing}$ for the five experimental secondary air flow rates were determined from Eq. (4.7a) based on the best-fit values of η shown in Figs. 5.13(a) and (b). Subsequently, the plot of $\dot{m}_{ing}$ was extrapolated to zero with respect to c_w to obtain $c_{w,min}$.

Estimation of Asymptote Value of Egress Discharge Coefficient at $c_w = c_{w,min}$

From Eq. (4.7a), when $\eta = 1$, $\dot{m}_{ing} = 0$. From Eq. (4.5a), when $\dot{m}_{ing} = 0$, $C_{di} = 0$. From Eq. (4.8b), at $c_w = c_{w,min}$,

$$(C_{de})_{at\ c_w=c_{w,min}} = \frac{c_{w,min}\mu R_h}{A_{gap}(\Delta a_{egress})_{at\ c_w=c_{w,min}}(2\rho)^{0.5}} \qquad (4.9)$$

In the above equation, $\left(\Delta a_{egress}\right)_{at\ c_w=c_{w,min}}$ is the only unknown. The plot of Δa_{egress} vs c_w was extrapolated to $c_w = c_{w,min}$ to obtain the value of $\left(\Delta a_{egress}\right)_{at\ c_w=c_{w,min}}$.

4.3 Estimation of Discharge Coefficients at Zero Purge Flow Rate

The sealing effectiveness is zero at zero purge flow rate. Ingestion and egress will occur because of pressure asymmetry in the main gas annulus and disk pumping. The ingestion and egress discharge coefficients will have definite values.

Using Eq. (**4.6**) in Eq. (**4.8a**),

$$C_{di} = \left[\frac{\dot{m}_{purge} + \dot{m}_{ing}}{\dot{m}_{purge}} - 1\right]\frac{\dot{m}_{purge}}{\Delta a_{ing}A_{gap}(2\rho)^{0.5}}$$

At $c_w = 0$,

$$C_{di} = \frac{\dot{m}_{ing}}{\Delta a_{ing}A_{gap}(2\rho)^{0.5}} \tag{4.10}$$

For estimating $(C_{di})_{at\ c_w=0}$, the plots of $\dot{m}_{ing}$ and Δa_{ing} were extrapolated to $c_w = 0$ to obtain the values $\left(\dot{m}_{ing}\right)_{at\ c_w=0}$ and $\left(\Delta a_{ing}\right)_{at\ c_w=0}$. The corresponding ingestion discharge coefficient is therefore given by,

$$(C_{di})_{at\ c_w=0} = \frac{\left(\dot{m}_{ing}\right)_{at\ c_w=0}}{\left(\Delta a_{ing}\right)_{at\ c_w=0}A_{gap}(2\rho)^{0.5}} \tag{4.11}$$

43

Similarly, the egress discharge coefficient is given by,

$$\left(C_{de}\right)_{\text{at } c_w=0} = \frac{\left(\dot{m}_{ing}\right)_{\text{at } c_w=0}}{\left(\Delta a_{egress}\right)_{\text{at } c_w=0} A_{gap}(2\rho)^{0.5}} \qquad (4.12)$$

CHAPTER 5

RESULTS AND DISCUSSION

Pressure and ingestion experiments were carried out at the conditions listed in Table **5.1** to characterize ingestion through the rim seal of the axial flow turbine stage (Fig. **3.3**). For the two different main air flow conditions, β_2 was

Exp. set	Main air flow rate (cfm / $Re_{v_{ax}}$ / Re_{R_h})	Rotor Speed (rpm / Re_ϕ)	Purge air flow rate (cfm / c_w)	β_2 (°)	Purge flow rate / main air flow rate (%)	V_{ax}/U	Free Disk pumping flow rate (cfm / $c_{w,fd}$)	λ_{turb}
I	2300 / 1.12×10^5 / 4.54×10^5	2400 / 6.14×10^5	5 / 769	48.3	0.217	0.74	60.8 / 9352	0.018
			10 / 1538		0.435			0.036
			20 / 3076		0.870			0.072
			30 / 4613		1.304			0.108
			40 / 6151		1.739			0.144
II	1900 / 9.27×10^4 / 3.76×10^5	1900 / 4.85×10^5	5 / 769	49.7	0.263	0.78	50.4 / 7746	0.022
			10 / 1538		0.526			0.043
			20 / 3076		1.053			0.087
			30 / 4613		1.579			0.130
			40 / 6151		2.105			0.174

Table **5.1** Experimental Conditions

maintained at about the same value. The flow coefficient (V_{ax}/U) values of 0.74 and 0.78 for expt. set I and II respectively, are close to the value for an older-model aircraft engine (JT9D) stage from where the blade and vane shapes have been obtained. The rotational Reynolds (Re_ϕ) number is an order lower than the actual engine conditions.

The average laboratory ambient pressure was 101860 Pa (absolute) and the average laboratory temperature 23ºC during the experiments. The estimated uncertainties in the values of the nondimensional parameters Re_ϕ, Re_{R_h} and c_w are $\pm 0.5\%$, $\pm 1\%$ and $\pm 1.5\%$ respectively [32].

5.1 Time-averaged Static Pressure Measurement Results

The air drawn by the centrifugal main blower from laboratory ambient flows through the honeycomb section and enters the vane row which turn the flow by 68.6°. A circumferential pressure asymmetry is created because of blockage of the flow by the vanes; this asymmetry decays downstream of the vane trailing edge plane. This circumferential pressure asymmetry is a major driver of ingestion and the dependence of ingestion on the peak-to-trough pressure asymmetry amplitude is discussed later in this chapter.

Static pressure is measured over two vane pitches at two axial locations on the vane platform, viz. 1 mm downstream of the vane trailing edge plane and 1 mm upstream of the seal lip. On the outer shroud, static pressure is measured over two vane pitches, at 1 mm downstream of vane trailing edge plane, 5 mm downstream of vane trailing edge plane and 1 mm upstream of blade leading edge plane.

For brevity, only the results for expt. set I and II at $c_w = 1538$ are presented in Figs. **5.1(a)**, **(b)** and **5.2(a)**, **(b)**. The circumferential-average pressure at vane platform 1 mm downstream of vane trailing edge plane is seen to be lower than that at the corresponding location on the outer shroud. The swirl imparted to the flow by the vanes cause a radial pressure gradient, and this pressure increases

Fig. **5.1(a)** Circumferential Distributions of Static Pressure at Main Gas Annulus Outer Shroud Over Two Vane Pitches for Three Axial Positions - Expt. Set I Condition $c_w = 1538$

Fig. **5.1(b)** Circumferential Distributions of Static Pressure at Vane Platform and in Rim Cavity at Stator Surface - Expt. Set I Condition $c_w = 1538$
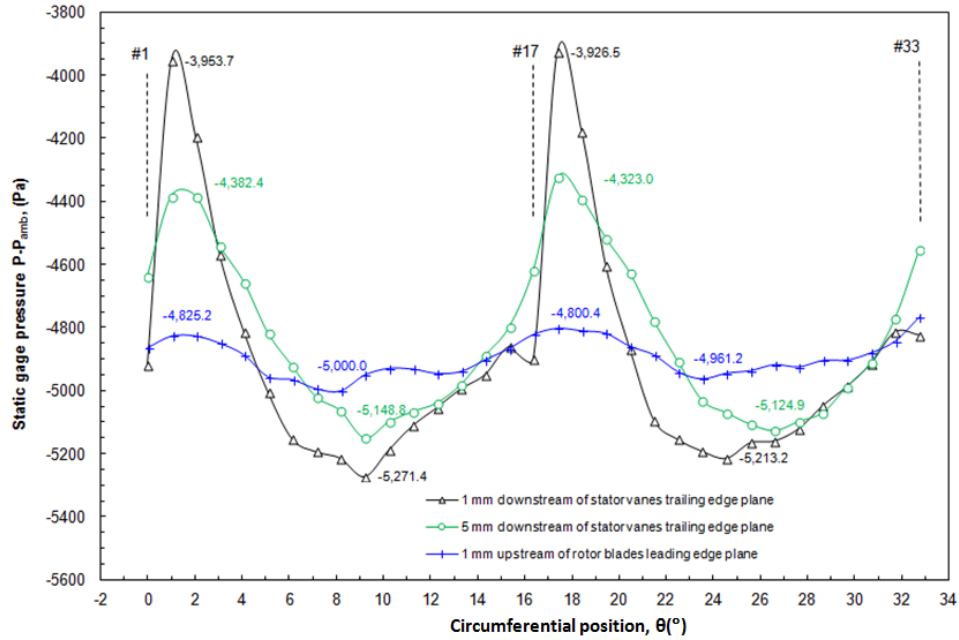
Fig. **5.2(a)** Circumferential Distributions of Static Pressure at Main Gas Annulus Outer Shroud Over Two Vane Pitches for Three Axial Positions - Expt. Set II Condition $c_w = 1538$
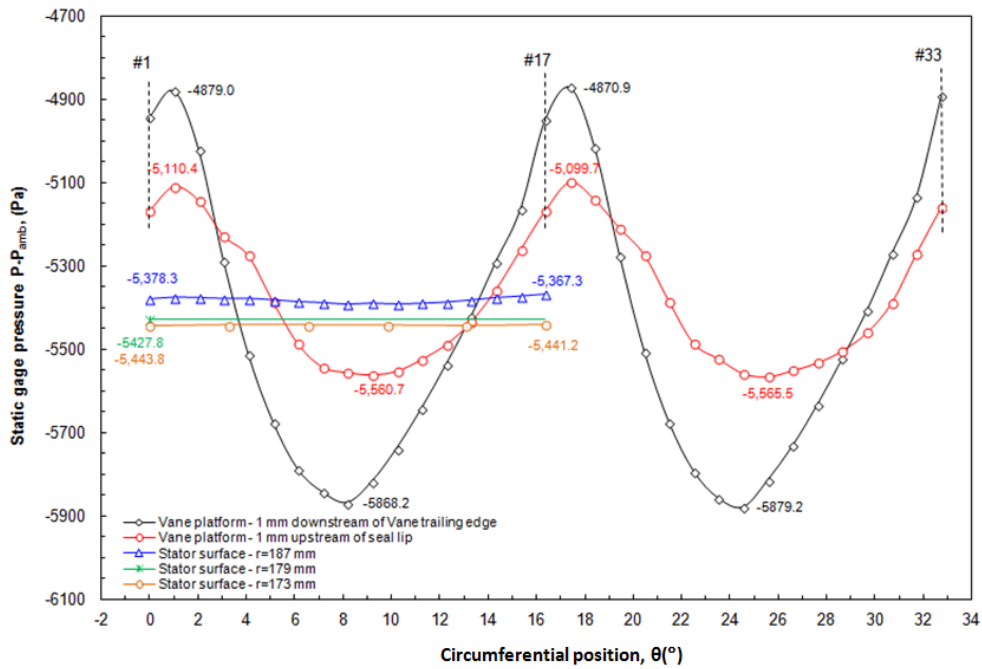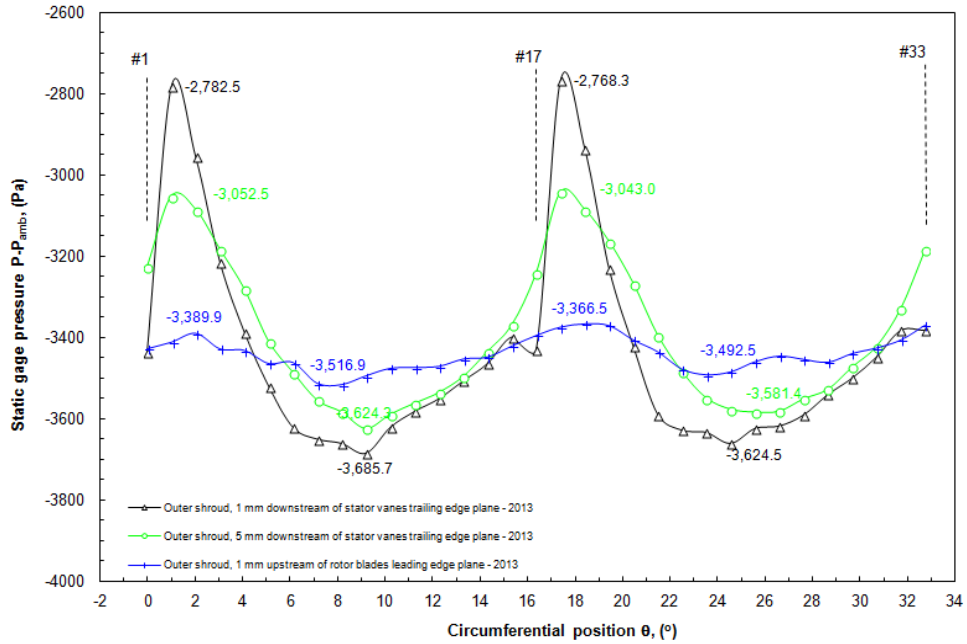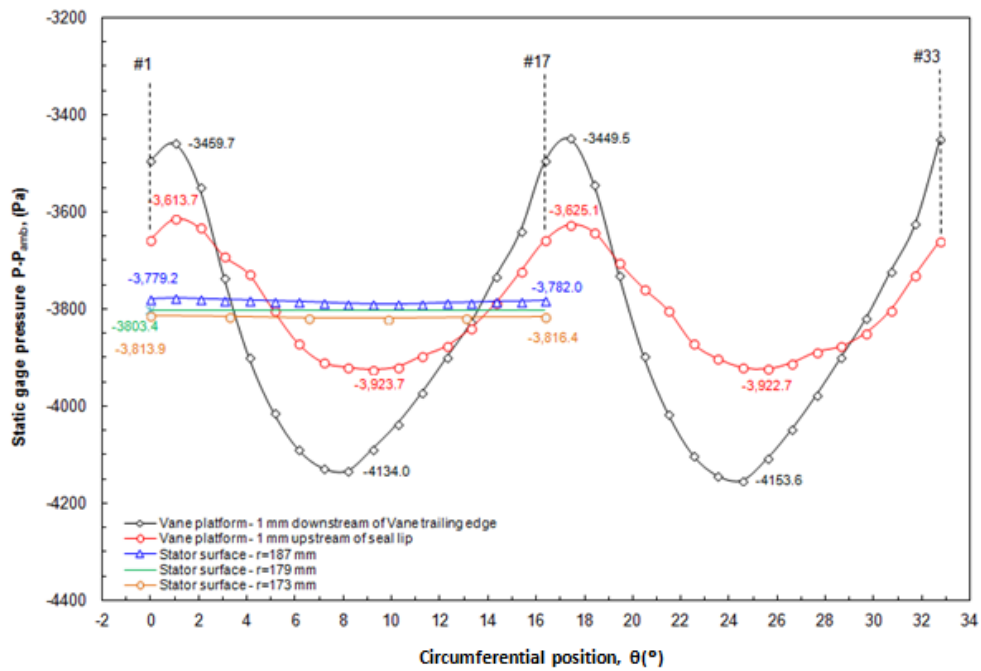

Fig. **5.2(b)** Circumferential Distributions of Static Pressure at Vane Platform and in Rim Cavity at Stator Surface - Expt. Set II Condition $c_w = 1538$

48

radially. The same trend is observed for the peak-to-trough pressure amplitude; also, this amplitude decays downstream of the vane trailing edge plane.

The peak-to-trough pressure asymmetry amplitude decreases with decrease in the main air flow rate. In the rim cavity, a very small circumferential pressure asymmetry exists at the radial location 187 mm (this is the seal region), while there is none at the radial location 173 mm.

Figures **5.3** and **5.4** show the effect of purge air flow rate on the static pressure distribution at the outer shroud for three axial locations. Although the ratio of purge air flow rate to the main air flow rate is quite small (Table **5.1**), the pressure levels decrease slightly with increase in the purge air flow rate.

The purge air flow rate has noticeable effect on the static pressure level and the peak-to-trough pressure asymmetry amplitude at 1 mm upstream of the seal lip. In the rim cavity, at radial location 187 mm, the pressure level increases with the purge flow rate. These two pressure locations are important as the ingestion and egress are considered to be driven by the pressure differential between these locations, Fig. **4.1**. Figures **5.5** and **5.6** contain the circumferential distributions of static pressure over one vane pitch at five purge air flow rates at r = 187 mm and at 1 mm upstream of seal lip. As mentioned earlier, the peak-to-trough pressure asymmetry in the main annulus decreases and the static pressure level in the rim cavity at r = 187 mm increases as the purge air flow rate increases. The peak-to-trough pressure asymmetry decrease with the increase in purge air

49
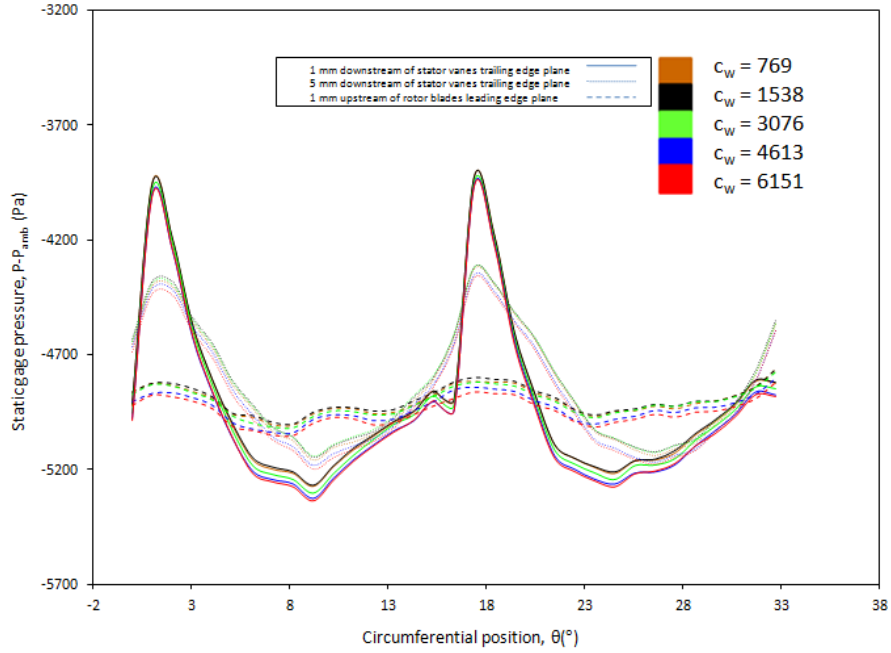
Fig. **5.3** Effect of Purge Air Flow Rate on the Circumferential Distributions of Time-averaged Static Pressure at Main Gas Annulus Outer Shroud Over Two Vane Pitches for Three Axial Positions - Expt. Set I
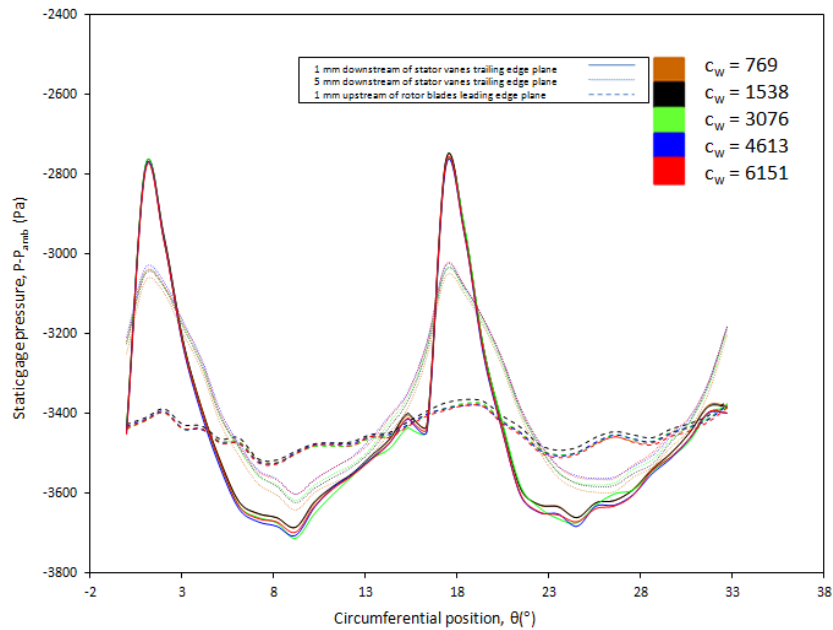
Fig. **5.4** Effect of Purge Air Flow Rate on the Circumferential Distributions of Time-averaged Static Pressure at Main Gas Annulus Outer Shroud Over Two Vane Pitches for Three Axial Positions - Expt. Set II
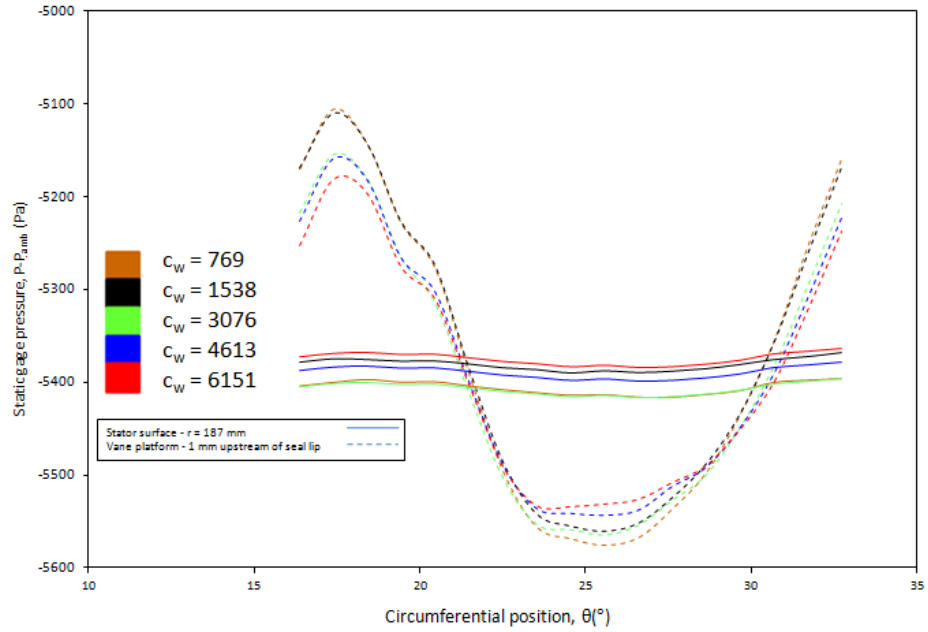
Fig. **5.5** Effect of c_w on the Circumferential Distributions of Time-averaged Static Pressure on Vane Platform (1 mm Upstream of Seal Lip) and Radial Location 187 mm ($r/R_h = 0.955$) for Expt. Set I
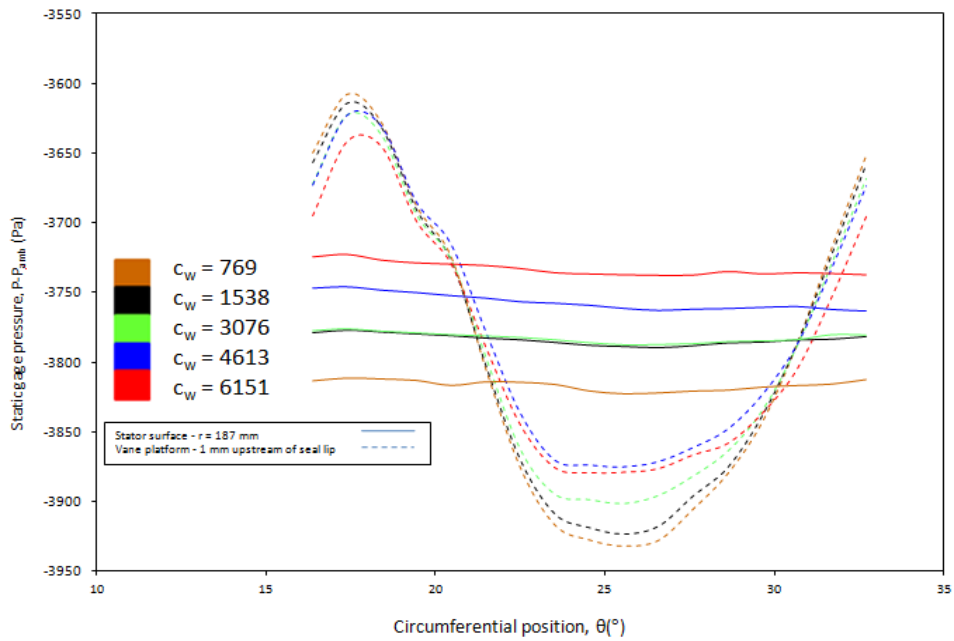
Fig. **5.6** Effect of c_w on the Circumferential Distributions of Time-averaged Static Pressure on Vane Platform (1 mm Upstream of Seal Lip) and Radial Location 187 mm ($r/R_h = 0.955$) for Expt. Set II

51
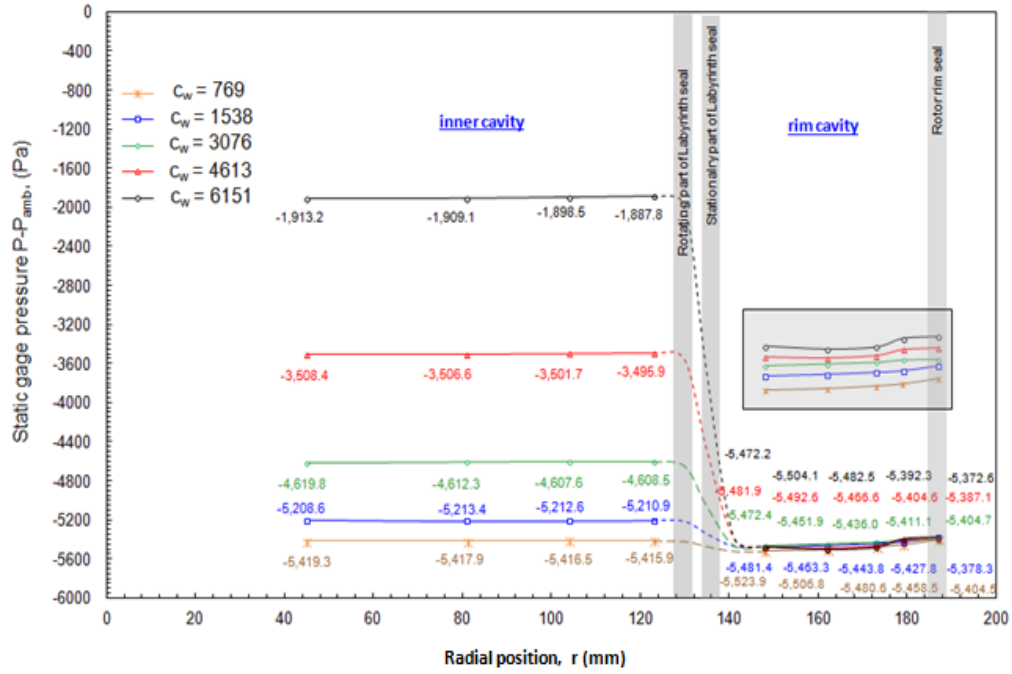
Fig. **5.7** Radial Distributions of Static Pressure in Rim and Inner Cavities at Stator Surface - Expt. Set I Conditions
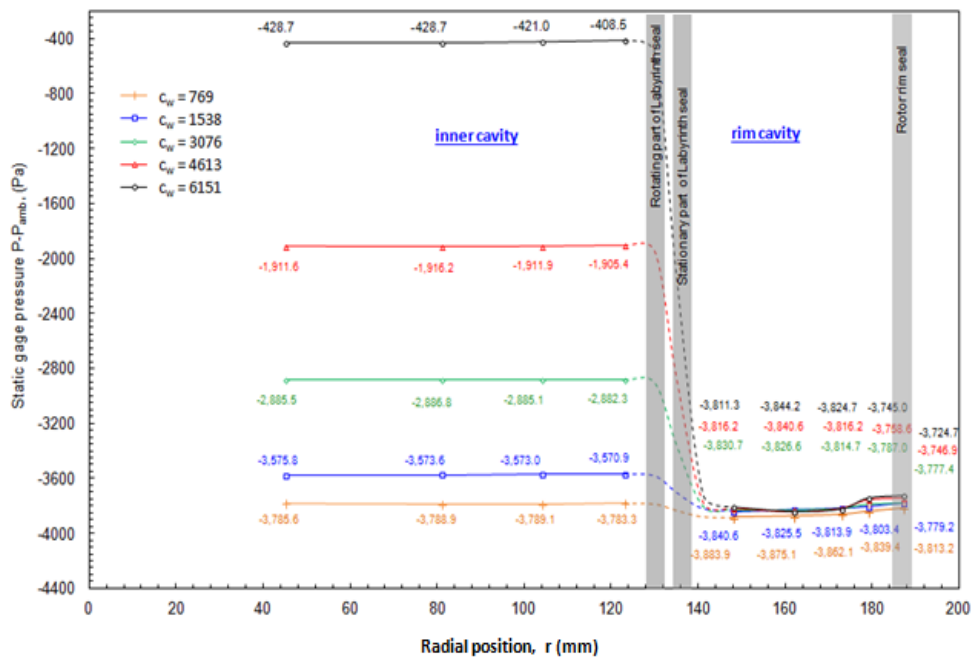
Fig. **5.8** Radial Distributions of Static Pressure in Rim and Inner Cavities at Stator Surface - Expt. Set II Conditions

flow rate possibly because of the interaction of rim cavity egress flow with the main flow.

Figures **5.7** and **5.8** contain the radial distributions of static gage pressure for expt. set I and II respectively. The distributions of static pressure in the inner cavity are essentially uniform. The pressure level rises in the inner cavity with the increase in purge air flow rate, primarily because of the restriction of flow due to the labyrinth seal. Although the pressure in the rim cavity does not vary appreciably with change in purge air flow rate, the shape of the pressure distribution near the rim seal radially outboard of r ≈ 172 mm qualitatively points to the potential for ingestion of main air from the annulus into the rim cavity (see inset in Fig. **5.7**). The potential for ingestion at higher purge air flow rate is lower than at lower purge air flow rate as the radial gradient of pressure radially inboard of the rim seal is lower for higher purge air flow rate.

5.2 Time-averaged Ingestion Measurement Results

The ingestion of main air from the annulus into the disk cavity is countered by the combined effects of rim seal and purge air. The time-averaged local sealing effectiveness, η(r), is defined by Eq. (**3.5**). As discussed earlier, the volumetric concentration of tracer gas (CO_2) in purge air was measured 0.38 m upstream of the disk cavity entrance. For the two lowest purge air flow rates, this tracer gas concentration was measured to be the same as the concentration at the innermost radial location (r = 45 mm) in the disk inner cavity, indicating full mixing of tracer gas with the purge air prior to entering the cavity. However, for

the three higher purge air flow rates, the concentrations at these two locations were different, indicating incomplete mixing. For the calculation of $\eta(r)$, the η-value at $r = 45$ mm was considered to represent C_{purge}, for all purge air flow rates; this implies that mixing was complete post-90º turn of the purge air in reaching the $r = 45$ mm location.

Figures **5.9** and **5.10** show the radial distributions of local sealing effectiveness at the stator surface for the expt. sets I and II respectively. For both sets, the distributions are uniform in the inner cavity which is completely sealed as well. It is observed that the sealing effectiveness in the rim cavity is lower for expt. set I as compared to expt. set II. Experiment set I features higher main air flow rate and higher disk rotational speed; this leads to greater peak-to-trough pressure asymmetry amplitude in the main gas path and greater disk-pumping for expt. set I. As such, the lower sealing effectiveness in the rim cavity for expt. set I is reasonable. Figure **5.11(a)** shows the variation of local sealing effectiveness on the stator surface at radial location 179 mm ($r/R_h = 0.915$) with purge air flow rate for expt. sets I and II. The 179 mm location is thought to be at the interface between the 'mixing region' and the 'beginning of the stator boundary layer' [9]. It is also observed that the sealing effectiveness increases sharply at lower values of c_w and then increases only by small amounts at higher values of c_w.

Figure **5.11(b)** shows the distribution of sealing effectiveness versus $\left[c_w / 2\pi G_c Re_\phi \right]$ for both sets of experiments at three radial locations, viz.
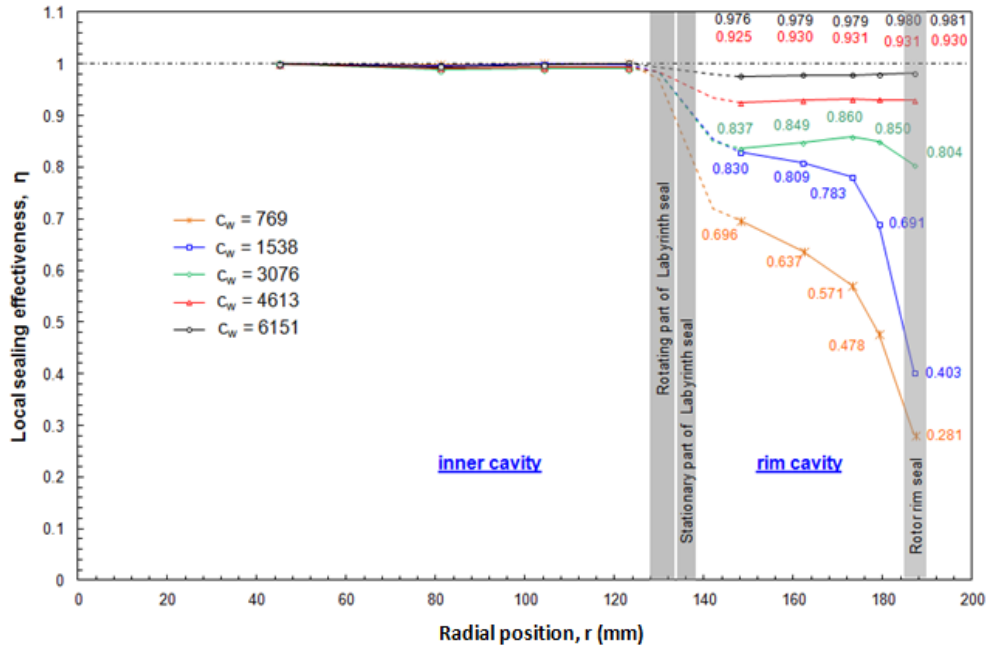
Fig. **5.9** Radial Distributions of Local Sealing Effectiveness in Rim and Inner
Cavities at Stator Surface - Expt. Set I Conditions
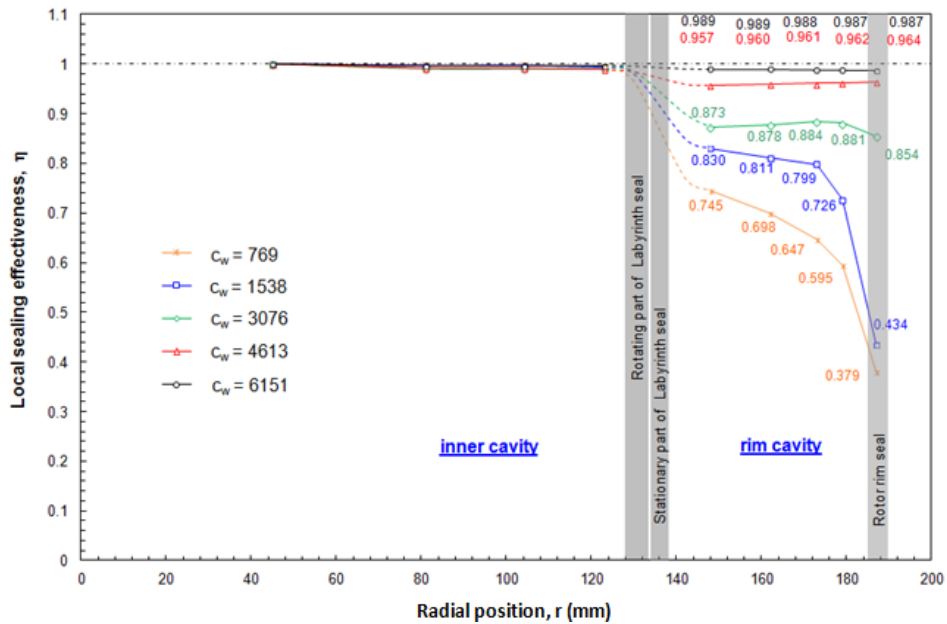
Fig. **5.10** Radial Distributions of Local Sealing Effectiveness in Rim and Inner
Cavities at Stator Surface - Expt. Set II Conditions
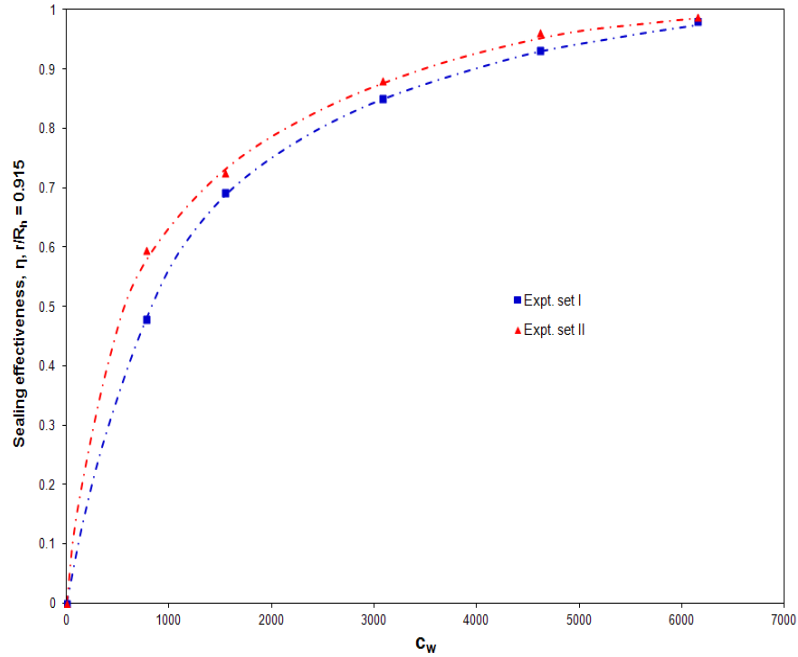
Fig. **5.11(a)** Sealing Effectiveness at r = 179 mm (r/R$_h$ = 0.915) on Stator Surface Versus Purge Flow Rate
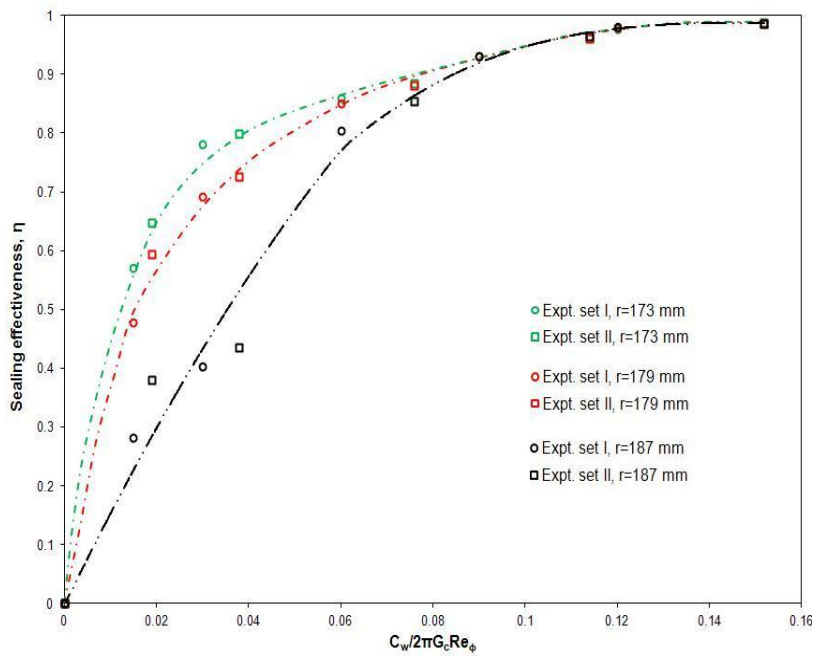
Fig. **5.11(b)** Sealing Effectiveness at r = 173 mm, 179 mm and 187 mm (r/R$_h$ = 0.884, 0.915 and 0.955 respectively) on Stator Surface Versus $C_W/2\pi G_C Re_\Phi$. Also Shown are the Best-Fit Lines for the Data
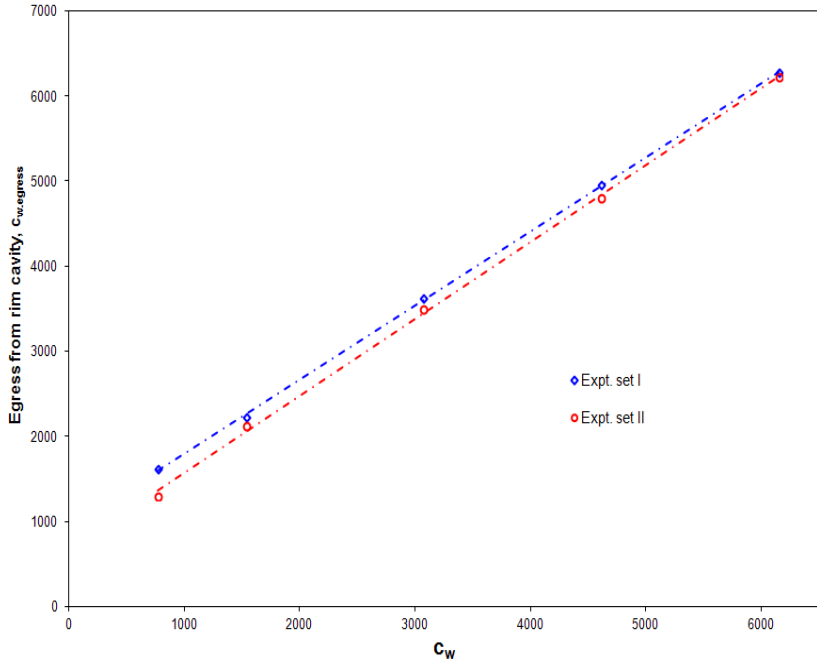
Fig. **5.12(a)** Egress from Rim Cavity Versus Purge Air Flow Rate Based on η-Values at r = 179 mm (r/R_h = 0.915)
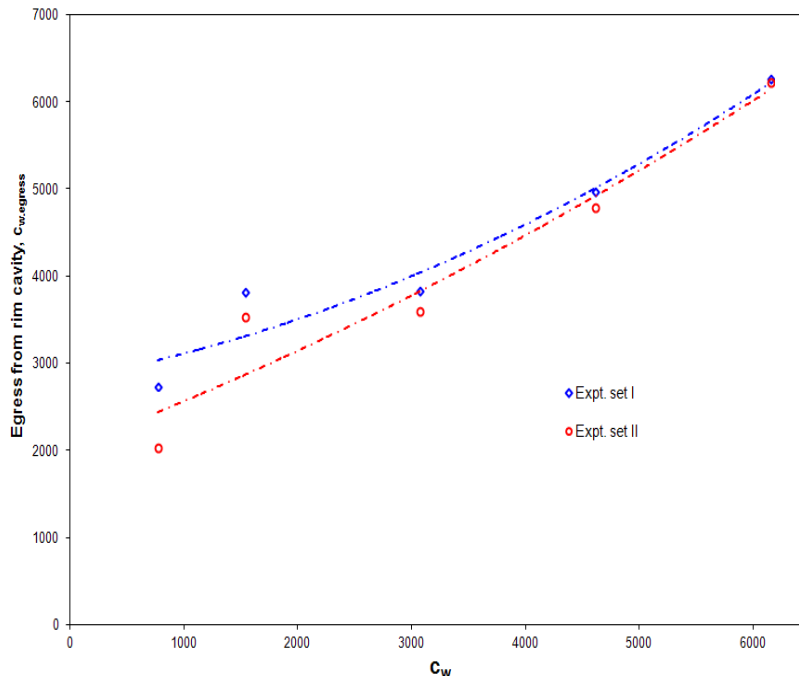
Fig. **5.12(b)** Egress from Rim Cavity Versus Purge Air Flow Rate Based on η-Values at r = 187 mm (r/R_h = 0.955)

57

173 mm, 179 mm and 187 mm. The sealing effectiveness values for the two sets collapse on a single curve (shown by dashed lines) at each thee radial location. Some scatter is seen at lower values of $\left[c_w/2\pi G_c Re_\phi\right]$ at the 187 mm location, quite possibly because this location is in the seal region where the flow is more disturbed than at the two radially inboard locations.

The egress flow from the rim cavity into the annulus is comprised of the ingested air and the purge air. Equation (**4.7b**), can be re-written as,

$$c_{w,egress} = \frac{c_w}{\eta} \qquad\qquad (5.1)$$

Figures **5.12(a), (b)** show plots, versus the purge flow rate, of egress from the rim cavity for both experiment sets calculated using sealing effectiveness values at r = 179 mm and 187 mm. The plots are concave up, implying that $c_{w,egress}$ increases monotonically with the purge air flow rate. Also, the $c_{w,egress}$ for expt. set I is consistently higher than for expt. set II for all purge flows; this is because for a given purge flow, the ingestion in expt. set I is greater than expt. set II. For higher c_w values, $c_{w,egress}$ for the two sets show a converging trend; note that the corresponding sealing effectivenesses also converge at higher values of c_w (Fig. **5.11(a)**).

5.3 Ingestion and Egress Discharge Coefficients

The ingestion and egress discharge coefficients are calculated using Eqs. (**4.8a**) and (**4.8b**) respectively. Figures **5.13(a)**, **(b) and 5.14(a)**, **(b)** show the
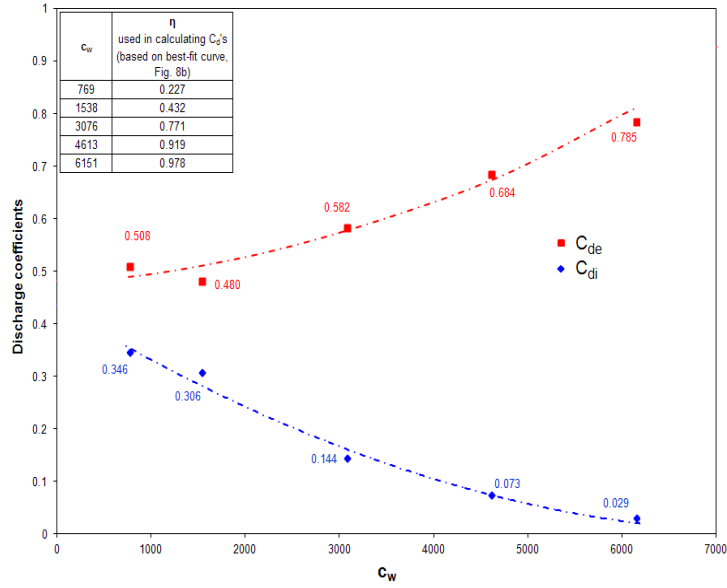
(a) Expt. set I
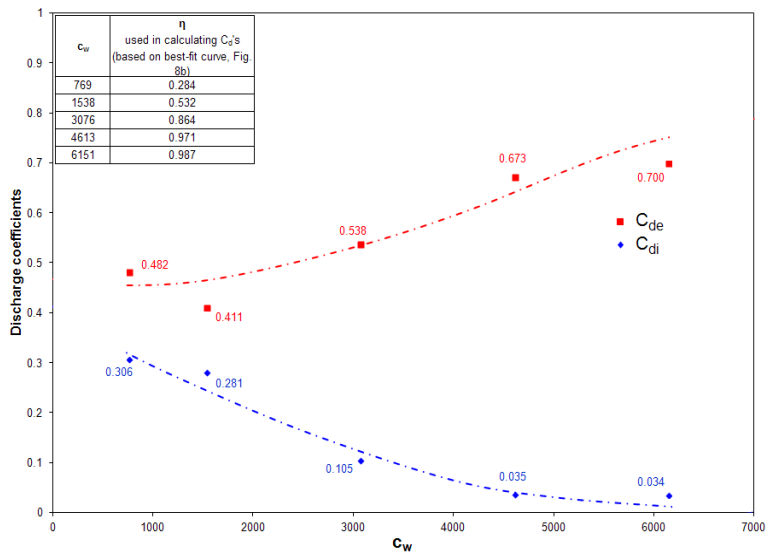
(b) Expt. set II

Fig. **5.13** Ingestion and Egress Discharge Coefficients Based on Rim Cavity Location r = 187 mm (r/R_h = 0.955) (The η-Values Obtained from the Best-Fit Line in Fig. **5.11(b)** (Inset Table) are used to Calculate the Discharge Coefficients. Note: The Lines Drawn Through the Discharge Coefficient Values Only Indicate the Data Trend)
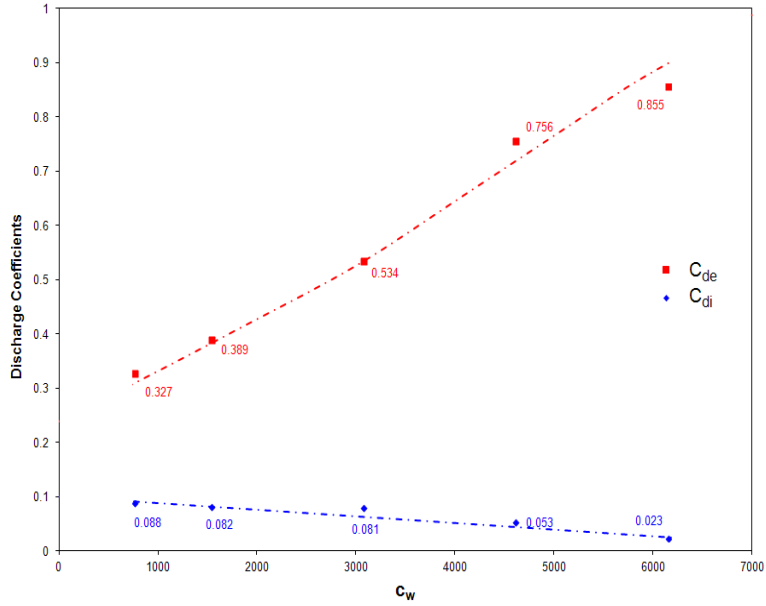
(a) Expt. set I
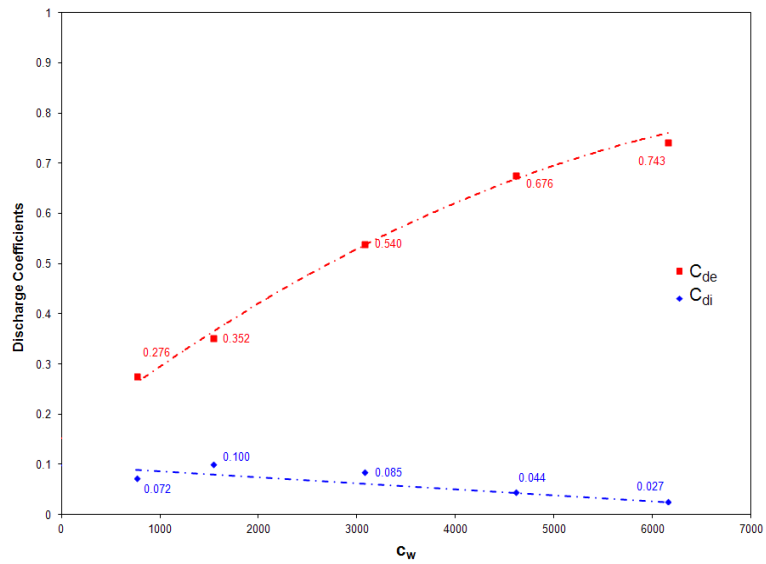
(b) Expt. set II

Fig. **5.14** Ingestion and Egress Discharge Coefficients Based on Rim Cavity Location r = 179 mm (r/R_h = 0.915) (The Measured η-Values (Figs. **5.9** and **5.10**) are used to Calculate the Discharge Coefficients. Note: The Lines Drawn Through the Discharge Coefficient Values Only Indicate the Data Trend)

variation of C_{di} and C_{de} with purge air flow rate calculated on the basis of sealing effectiveness and static pressure values at the rim cavity radial locations 187 mm ($r/R_h = 0.955$) and 179 mm ($r/R_h = 0.915$), respectively. In both cases, main gas path pressure at 1 mm upstream of seal lip was used.

In Fig. **5.11(b)**, a considerable scatter is observed in the η-values at the location 187 mm for the lower two purge air flows. As such, the η-values obtained from the best-fit line are used for the calculation of discharge coefficients shown in Figs. **5.13(a)**, **(b)**; the η-values used are given in the inset table of each figure. For the calculation of C_{di} and C_{de} corresponding to the location 179 mm, the measured values of sealing effectiveness were used as the scatter in η-values at this radial location is small even for the lower purge air flow rates. For both experiment sets, the egress discharge coefficient increases with purge air flow rate whereas the ingestion discharge coefficient decreases with purge air flow rate. The egress discharge coefficients shown in Figs. **5.14(a)**, **(b)** have a similar trend to those in Figs. **5.13(a)**, **(b)**; the ingestion discharge coefficient decreases only slightly now.

The purpose of the preceding comparison is to point out the role of the radial location chosen in the rim cavity for sealing effectiveness and pressure values in the calculation of discharge coefficients. The choice of the rim cavity radial location is somewhat subjective; however, the radial location 187 mm (in the seal region) is preferred over 179 mm (in the cavity mixing region) in the present study. It is important to mention also that the choice of pressure location

in the main gas path is also subjective; a location very close to the vane platform lip is preferred in this study.

In an experimental study, there are geometrical constraints which render the pressure measurement at some critical locations in the stage impractical. On the other hand, a computational study (CFD) allows freedom of choice of the locations, such as anywhere on the vane platform and in the rim cavity. Steady state CFD simulations may be used in conjunction with the pressure and ingestion measurements in the laboratory. For a particular turbine stage set-up, a large set of discharge coefficient values corresponding to different combinations of main gas path location and rim cavity location can provide some guidelines for the most suitable locations for the calculation of discharge coefficients.

Figures **5.15(a)**, **(b)** show the variation of the ratio C_{di}/C_{de} (discharge coefficients based on 187 mm location in the rim cavity) versus the purge air flow rate for the two experiment sets. The ratio is given by,

$$\frac{C_{di}}{C_{de}} = (1 - \eta)\frac{\Delta a_{egress}}{\Delta a_{ing}} \tag{5.2}$$

As the ratio varies between the values 0.04 to 0.70, its dependence on purge air flow rate cannot be ignored.

The method of estimation of $c_{w,min}$ is explained in section **4.2**. C_{di} is equal to zero; the egress discharge coefficient at $c_w = c_{w,min}$ is calculated using Eq.

(**4.9**). Table **5.2** gives the value of $c_{w,min}$ and the values of discharge coefficients at this secondary air flow rate, for both experiment sets.

	Expt. Set I	Expt. Set II
$c_{w,min}$	7997	7045
C_{di}	0	0
C_{de}	0.983	0.798

Table **5.2** $c_{w,min}$ Values along with Corresponding Discharge Coefficients for Both Experiment Sets

The method of estimation of discharge coefficients at zero secondary air flow rate is explained in section **4.3**. η is equal to zero now; the ingestion and egress discharge coefficients are calculated using Eqs. **4.11** and **4.12,** respectively. The discharge coefficient ratio calculated using Eq. **5.2** is given by,

$$\left(\frac{C_{di}}{C_{de}}\right)_{c_w=0} = \left(\frac{\Delta a_{egress}}{\Delta a_{ing}}\right)_{c_w=0} \qquad (5.3)$$

Note that the ingestion and egress discharge coefficient ratio at zero purge air flow rate can be found simply from the time-averaged static pressure measurements. Table **5.3** provides the values of discharge coefficients and their ratio at zero secondary air flow rate for both experiment sets.

	Expt. Set I	Expt. Set II
C_{di}	0.432	0.415
C_{de}	0.498	0.483
C_{di}/C_{de}	0.867	0.859

Table **5.3** Discharge Coefficients and their Ratios at Zero Purge Air Flow Rate for both Experiment Sets
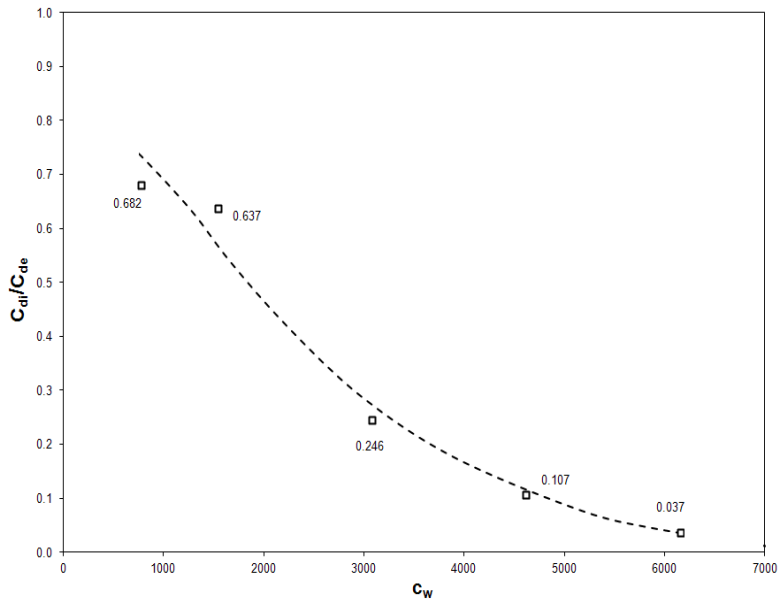
(a) Expt. set I
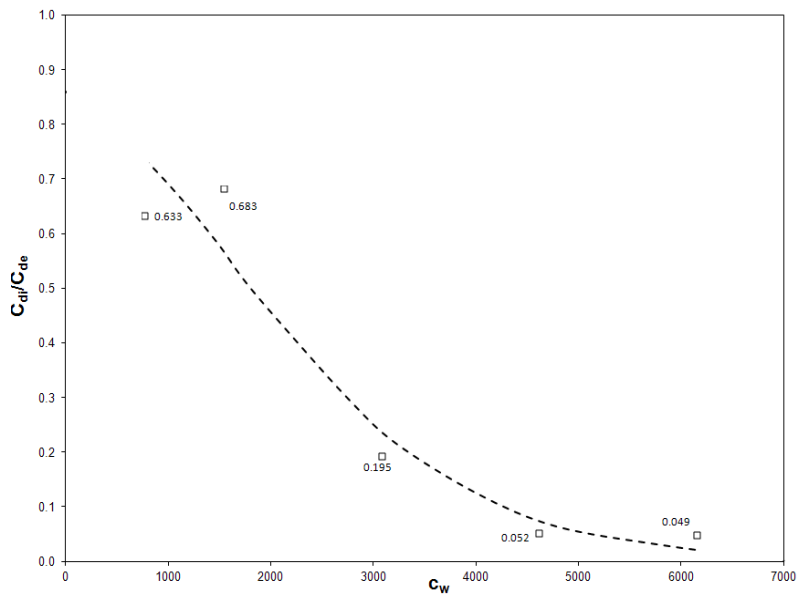
(b) Expt. set II

Fig. **5.15** Discharge Coefficient Ratio Versus Purge Air Flow Rate Based on Rim
Cavity Location r = 187 mm (r/R$_h$ = 0.955)

Ingestion and egress discharge coefficients for the two experiment sets are represented by a single curve (quadratic fit) in Fig. **5.16** in which the coefficients are plotted versus $V_{rim\ seal}/V_{ax}$. In Fig. **5.17**, the ingestion and egress discharge coefficients are plotted versus $V_{rim\ seal}/U$. The discharge coefficients plots, Figs. **5.16** and **5.17**, exhibit similar trends with respect to the non-dimensional parameters $V_{rim\ seal}/V_{ax}$ and $V_{rim\ seal}/U$.
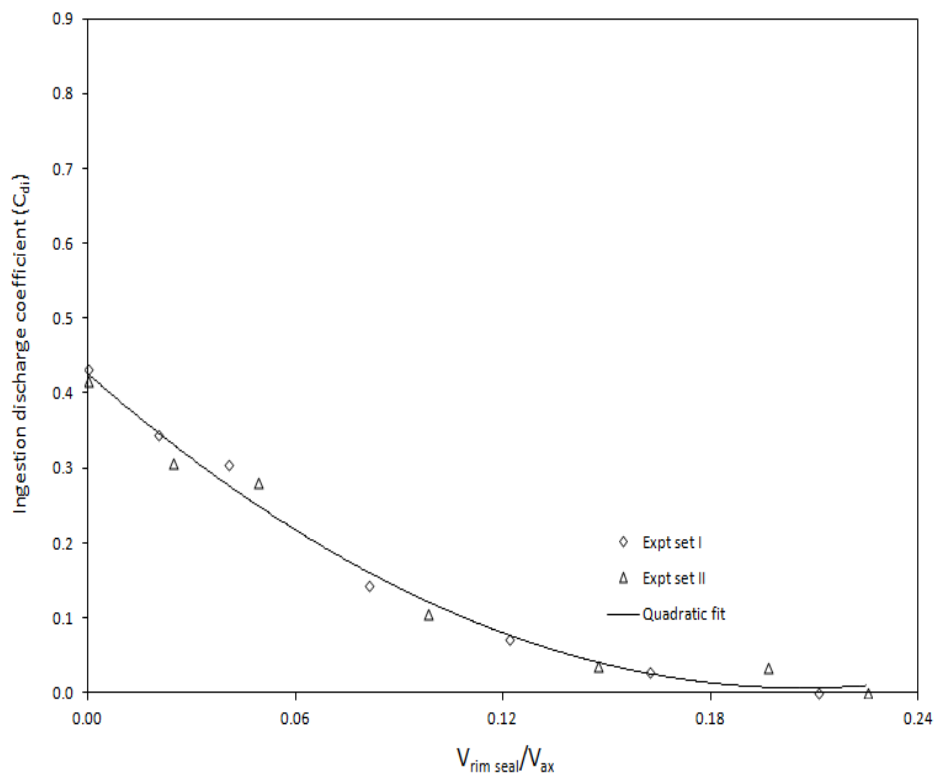
Fig. **5.16(a)** Ingestion Discharge Coefficients Based on Radial Location r = 187 mm (r/R$_h$ = 0.955) Versus $V_{Rim\ Seal}/V_{Ax}$
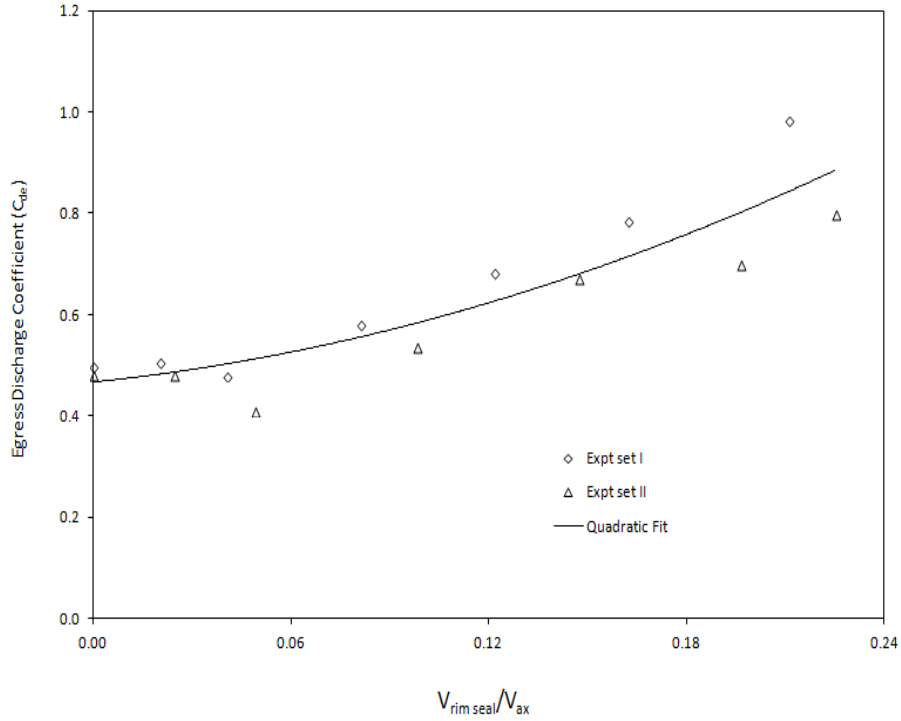
Fig. **5.16(b)** Egress Discharge Coefficients Based on Radial Location r = 187 mm
(r/R_h = 0.955) Versus $V_{Rim\ Seal}/V_{Ax}$
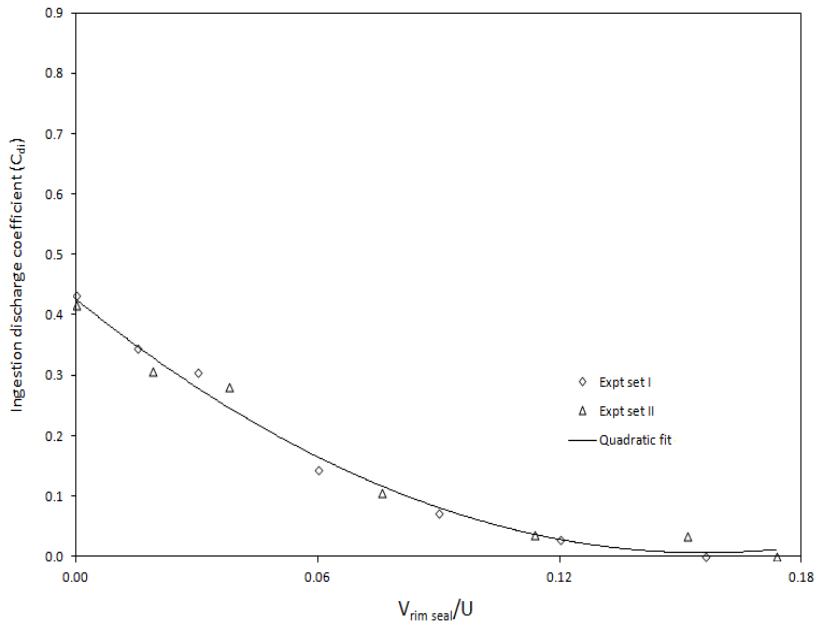
Fig. **5.17(a)** Ingestion Discharge Coefficients Based on Radial Location r = 187
mm (r/R_h = 0.955) Versus $V_{Rim\ Seal}/U$
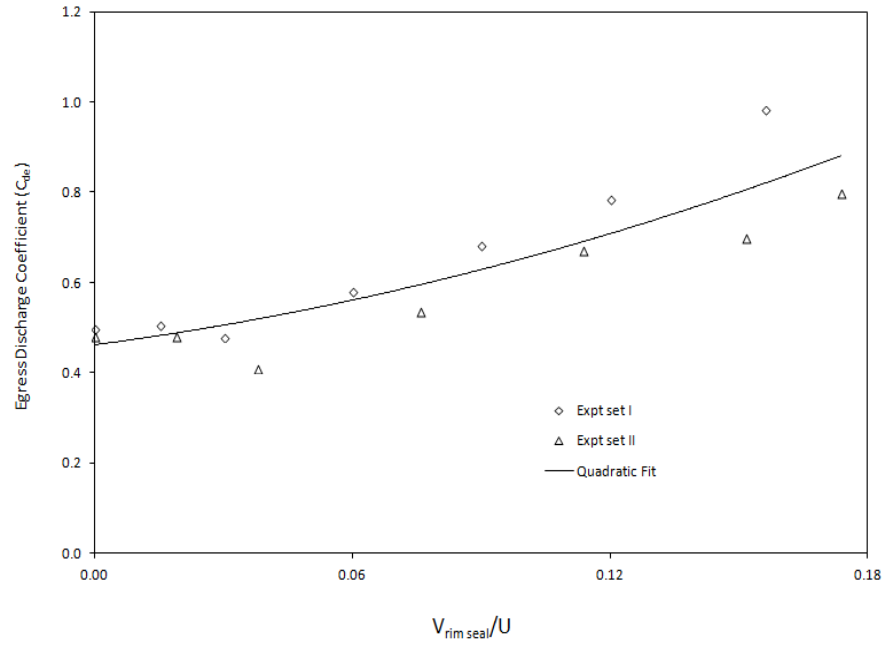
Fig. **5.17(b)** Egress Discharge Coefficients Based on Radial Location r = 187 mm
(r/R_h = 0.955) Versus $V_{Rim\ Seal}$/U

CHAPTER 6

CONCLUDING REMARKS AND SUGGESTIONS FOR FUTURE RESEARCH

6.1 Concluding Remarks

Experiments were performed on a subscale single-stage axial turbine featuring vanes, blades, an axially-overlapping radial rim seal clearance, and a labyrinth seal inboard of the disk cavity. The labyrinth seal divides the disk cavity into a rim cavity and an inner cavity. Time-averaged static pressure distributions at multiple locations in main gas annulus and disk cavity as well as local sealing effectiveness values based on tracer gas volumetric concentration measurements at several radial locations on the stator surface are reported.

The static pressure was essentially uniform radially in the inner cavity; variation was observed in the rim cavity, however. The radial pressure distribution near the rim seal qualitatively point toward the potential for main gas ingestion. In the 'cavity mixing region', the pressure distribution was circumferentially uniform; a small asymmetry was observed in the distribution in the 'seal region'. This is possibly caused by the interaction between the ingested air from the main annulus and the egress flow from the rim cavity. In the main annulus, circumferential pressure asymmetry was due to the presence of vanes and blades. The peak-to-trough pressure amplitude on the vane platform and the outer shroud decayed downstream from the vane trailing edge plane.

The radial distributions of local sealing effectiveness were uniform in the inner cavity; the inner cavity was completely sealed as well at the purge flow rates studied. In the rim cavity, the sealing effectiveness values for the experiment set featuring lower main air flow rate were consistently higher than those for the condition featuring higher main air flow rate. This was true for all radial locations and all purge flow rates.

The pressure and ingestion measurements were subsequently used to calculate the ingestion and egress discharge coefficients (C_{di} and C_{de}). Two sets of C_{di} and C_{de} values are reported for the rim seal - both use the pressure at the vane platform 1 mm upstream of seal lip along with the pressure and sealing effectiveness values at two radial locations in the rim cavity, one in the seal region and the other slightly inboard in the cavity mixing region. For both experiment sets, C_{di} decreased and C_{de} increased with purge air flow rate; C_{di} decreased only slightly for the radial location in the cavity mixing region. The location in the seal region is preferred over the location in the cavity mixing region for discharge coefficient calculations.

The ratio of discharge coefficients (C_{di}/C_{de}) varied significantly with purge air flow rates for both the experimental conditions. It is noteworthy that their ratio depends only on the pressure values in the main annulus and rim cavity for zero purge air flow.

It is acknowledged that the choice of pressure location in the main gas path, is to some extent, subjective; a location on the vane platform, very close to the lip of the seal is considered to be appropriate in this study.

A method of estimating $c_{w,min}$ was proposed; the values of $c_{w,min}$ for the experiments are reported. The $c_{w,min}$ values were only slightly higher than the maximum purge air flow rates for both set of experiments. Also, the egress discharge coefficient values at $c_w = c_{w,min}$ are reported.

The non-dimensional ratio, $[V_{rim\,seal}/V_{ax}]$ $(= \alpha)$, includes important rig dimensions which define the annulus area and rim seal clearance, along with the air properties at laboratory ambient condition. A plot between sealing effectiveness (η) and α for different experimental conditions collapse on to a single curve; this curve can be extrapolated to $\eta = 1$, and the corresponding value of α $(=\alpha_0)$ can be used in the determination of $c_{w,min}$ for a range of Re_{R_h} values. The relation between $c_{w,min}$ and Re_{R_h} is given by, $c_{w,min} = \Gamma_0 Re_{R_h}$, where $\Gamma_0 = 2\pi G_c \alpha_0$. Note that Γ_0 is a rig-specific parameter and hence, it has a unique value for a particular test rig. It is important to point out that this method of estimation of $c_{w,min}$ can be used only for the case of external flow dominated ingestion, wherein $c_{w,min}$ is independent of rotational Reynolds number (Re_ϕ) and depends only on the main air flow Reynolds number (Re_{R_h}). Since at engine conditions, hot mainstream gas ingestion into the disk cavity is externally induced, one value of Γ_0 can be helpful in the estimation of $c_{w,min}$ for a range of Re_{R_h} values without actually conducting experiments at each value of Re_{R_h}.

6.2 Suggestions for Future Research

The following should be considered:

- Unsteady pressure measurements for more accurate determination of ingestion.
- Use of steady CFD simulation pressure results in conjunction with time-averaged tracer gas concentration measurements, for the calculation of discharge coefficients based on different combinations of locations on vane platform and in the rim cavity. This may provide a guideline for the most suitable locations in main gas path and in the rim cavity for pressure and sealing effectiveness.

REFERENCES

[1]   Han, J.C., and Rallabandi, A.P., 2010, "Turbine Blade Film Cooling Using PSP Technique", Frontiers in Heat and Mass Transfer (FHMT), 1, 013001.

[2]   "Airplane Flying Handbook", U.S. Department of Transportation, Federal Aviation Administration, FAA-H-8083-3A.

[3]   Philip, H., and Peterson, C., (1992), "Mechanics and Thermodynamics of Propulsion", Second Edition, ISBN 0201146592.

[4]   Owen, J.M., and Rogers, R.H., 1989, "Flow and Heat Transfer in Rotating Disc Systems, Vol. 1: Rotor-Stator Systems, ISBN 0863800904.

[5]   Batchelor, G.K., 1951, "Note on a Class of Solutions of the Navier-Stokes Equations Representing Steady Rotationally-Symmetric Flow", Quarterly Journal of Mechanics and Applied Mathematics, Vol. 4, pp. 29-41.

[6]   Stewartson, K., 1953, "On the Flow Between Two Rotating Coaxial Discs", Mathematical Proceeding of the Cambridge Philosophical Society, Vol. 49, pp. 333-341.

[7]   Daily, J.W., and Nece, R.E., 1960, "Chamber Dimension Effects on Induced Flow and Frictional Resistance of Enclosed Disks", ASME Journal of Basic Engineering, pp. 217-232.

[8]   Childs, P.R.N., 2010, "Rotating Flow", ISBN 0123820987.

[9]   Johnson, B.V., Wang, C.-Z., and Roy, R.P., 2008, "A Rim Seal Orifice Model with Two Cds and Effects of Swirl in Seals", ASME Paper GT2008-50650.

[10]   Bayley, F.J., and Owen, J.M., 1969, "Flow Between a Rotating and a Stationary Disc", Aeronautical Quarterly 20, pp. 333-354.

[11]   Bayley, F.J., and Owen, J.M., 1970, "Fluid Dynamics of a Shrouded Disk System With a Radial Outflow of Coolant", Journal of Engineering and Power, pp. 335-341.

[12]   Phadke, U.P. and Owen, J.M., 1988, "Aerodynamic Aspects of the Sealing of Gas-Turbine Rotor0Stator Systems: Part I: The Behavior of Simple Shrouded Rotating-Disk Systems in Quiescent Environment", International Journal of Heat and Fluid Flow, Vol. 9(2), pp. 98-105.

[**13**]   Phadke, U.P. and Owen, J.M., 1988, "Aerodynamic Aspects of the Sealing of Gas-Turbine Rotor-Stator Systems: Part II: The Performance of Simple Seals in a Quasi-Axisymmetric External Flow", International Journal of Heat and Fluid Flow, Vol. 9(2), pp. 106-112.

[**14**]   Phadke, U.P. and Owen, J.M., 1988, "Aerodynamic Aspects of the Sealing of Gas-Turbine Rotor-Stator Systems: Part III: The Effects of Nonaxisymmetric External Flow on Seal Performance", International Journal of Heat and Fluid Flow, Vol. 9(2), pp. 113-117.

[**15**]   Phadke, U.P. and Owen, J.M., 1983, "An Investigation of Ingress for an Air Cooled Shrouded Rotating-Disk System with Radial-Clearance Seals", Journal of Engineering for Power, Vol. 105(1), pp. 178-183.

[**16**]   Bhavnani, S.H., Khilnani, V.I., Tsai, L.-C., Khodadadi, J.M., and Goodling, J.S., 1992, "Effective Sealing of a Disk Cavity Using a Double-Toothed Rim Seal", ASME Paper 92-GT-379.

[**17**]   Ko, S.H., and Rhode, D.L., 1991, "Thermal Details in a Rotor-Stator Cavity at Engine Conditions", ASME Paper 91-GT-275.

[**18**]   Daniels, W.A., Johnson, B.V., Graber, D.J., and Martin, R.J., 1992, "Rim Seal Experiments and Analysis for Turbine Applications", ASME Journal of Turbomachinery, Vol. 114(2), pp. 426-432.

[**19**]   Chew, J.W., Dadkhah, S., and Turner, A.B., 1992, "Rim Sealing of Rotor-Stator Wheelspaces in the Absence of External Flow", ASME Journal of Turbomachinery, Vol. 114(2), pp. 433-438.

[**20**]   Chew, J.W., 1991, "A Theoretical Study on Ingress for Shrouded Rotating Disk Systems with Radial Outflow", ASME Journal of Turbomachinery, Vol. 113(1), pp. 91-97.

[**21**]   Chew, J.W., Green, T., and Turner, A.B., 1994, "Rim Sealing of Rotor-Stator Wheelspaces in the Presence of External Flow", International Gas Turbine and Aeroengine Congress and Exposition, ASME Paper 94-GT-126.

[**22**]   Johnson, B.V., Mack, G.J., Paolillo, R.E., and Daniels, W.A., 1994, "Turbine Rim Seal Gas Path Flow Ingestion Mechanism", AIAA Paper 94-2703.

[**23**]   Bayley, F.J., Childs, P.R.N., 1997, "Prediction of Ingress Rates to Turbine and Compressor Wheelspaces", International Journal of Heat and Fluid Flow, Vol. 18, pp. 218-228.

[**24**]   Hills, N.J., Chew, J.W., Turner, A.B., 2002, Computational and Mathematical Modeling of Turbine Rim Seal Ingestion", ASME Journal of Turbomachinery, Vol. 124, pp. 306-315.

[**25**]   Roy, R.P., Xu, G., Feng, J., and Kang, S., 2001, "Pressure Field and Mainstream Gas Ingestion in Rotor-Stator Disk Cavity", ASME Paper 2001-GT-564.

[**26**]   Roy, R.P., Feng, J., Narzary, D.P., Paolillo, R.E., 2005, "Experiment on Gas Ingestion Through Axial-Flow Turbine Rim Seals", ASME Journal of Engineering for Gas Turbines and Power, Vol. 127, pp. 573-582.

[**27**]   Roy, R.P., Devasenathipathy, S., Xu, G., and Zhao, Y., 1999, "A Study of the Flow Field in a Model Rotor-Stator Disk Cavity", ASME Paper 99-GT-246.

[**28**]   Roy, R.P., Xu, G., and Feng, J., 2000, "Study of Mainstream Gas Ingestion in a Rotor-Stator Disk Cavity", AIAA Paper 2000-3372.

[**29**]   Roy, R.P., Zhou, D.W., Ganesan, S., Wang, C.-Z., Paolillo, R.E., and Johnson, B.V., 2007, "The Flow Field and Main Gas Ingestion in a Rotor-Stator Disk Cavity", ASME Paper GT2007-27671.

[**30**]   Zhou, D.W., Roy, R.P., Wang, C.-Z., and Glahn, G.A., 2011, "Main Gas Ingestion in a Turbine Stage for Three Rim Cavity Configurations", ASME Journal of Turbomachinery, Vol. 133, pp. 031023-1 - 031023-12.

[**31**]   Balasubramanian, J., Junnarkar, N., Roy, R.P., Glahn, J.A., 2011, "Disk Cavity Purge Air Outflow into the Main Gas Path of a Model Turbine Stage", Experimental Thermal and Fluid Science, Vol. 38, pp. 266-269.

[**32**]   Balasubramanian, J., Pathak, P.S., Thiagarajan, J.K., Singh, P., Roy, R.P., Mirzamoghadam, A.V., 2014, "Experimental Study of Ingestion in the Rotor-Stator Disk Cavity of a Subscale Axial Turbine Stage", ASME Paper GT2014-25487.

[**33**]   Gentilhomme, O., Hills, N.J., Turner, A.B., Chew, J.W., 2003, Measurement and Analysis of Ingestion Through a Turbine Rim Seal", Journal of Turbomachinery, Vol. 125, pp. 505-512.

[**34**]   Bohn, D.E., Decker, A., Ohlendorf, N., Jakoby, R., 2006, "Influence of an Axial and Radial Rim Seal Geometry on Hot Gas Ingestion into the Upstream Cavity of a 1.5-Stage Turbine", ASME Paper GT2006-90453.

[**35**]   Sangan, C.M., Pountney, O.J., Zhou, K., Wilson, M., Owen, J.M., Lock, G.D., 2013, "Experimental Measurements of Ingestion Through Turbine Rim

Seals-Part I: Externally Induced Ingress", ASME Journal of Turbomachinery, Vol. 135, pp. 021012-1 - 021012-10.

[**36**]   Owen, J.M., 2010, "Theoretical Modeling of Hot Gas Ingestion Through Gas Turbine Rim Seals", 3rd International Symposium on Jet Propulsion and Power Engineering.

[**37**]   Zhou, K., Wood, S.N., Owen, J.M., 2013, "Statistical and Theoretical Models of Ingestion Through Turbine Rim Seals", ASME Journal of Turbomachinery, Vol. 135, pp. 021014-1 - 021-14-8.

[**38**]   Sangan, C.M., Pountney, O.J., Zhou, K., Owen, J.M., Wilson, M., Lock, G.D., 2013, " Experimental Measurements of Ingestion Through Turbine Rim Seals-Part II: Rotationally Induced Ingress", ASME Journal of Turbomachinery, Experimental Measurements of Ingestion Through Turbine Rim Seals-Part I: Externally Induced Ingress, ASME Journal of Turbomachinery, Vol. 135, pp. 021013-1 - 021013-9.

[**39**]   Thiagarajan, J.K., 2013, "Experimental Study of Pressure and Main Gas Ingestion Distributions in a Model Rotor-Stator Disk Cavity", M.S. Thesis, Arizona State University.

[**40**]   Pathak, P.S., 2013, "Experimental Study of the Flow Field in a Model Rotor-Stator Disk Cavity Using Particle Image Velocimetry", M.S. Thesis, Arizona State University.

[**41**]   Narzary, D.P., 2005, "Experimental Study of the Flow Field in a Model Rotor-Stator Disk Cavity", M.S. Thesis, Arizona State University.

[**42**]   Eckert, E.R.G., Goldstein, R.J., 1976, "Measurements in Heat Transfer, 2nd ed., Hemisphere Publishing Corporation, Washington, DC.

[**43**]   Teuber, R., Li, Y.S., Maltson, J., Wilson, M., Lock, G.D., Owen, J. M., 2012, "Computational Extrapolation of Turbine Sealing Effectiveness from Test Rig to Engine Conditions", ASME IGTI paper GT2012-68490.

[**44**]   Laitone, E.V., 1951, "New Compressibility Correction for Two-Dimensional Subsonic Flow", Journal of Aeronautical Science, Vol. 18, pp. 350.

[**45**]   Dring, R.P., Joslyn, H.J., Hardin, L.W., Wagner, J.H., 1982, "Turbine Rotor-Stator Interaction", Journal of Engineering and Power, Vol. 144, pp. 729-742.